

1
2
3
4
5
6
7
8
9
10
11
12
13
14
15
16
17
18
19
20
21
22
23
24
25
26
27
28
29

An automatic method for screening clouds and cloud shadows in optical satellite image time series in cloudy regions

Xiaolin Zhu^{a*}, Eileen H. Helmer^b

^a Department of Land Surveying and Geo-Informatics, The Hong Kong Polytechnic University, Hong Kong

^b International Institute of Tropical Forestry, USDA Forest Service, Río Piedras, Puerto Rico, 00926, USA

*Corresponding author:

Xiaolin Zhu

Address: The Hong Kong Polytechnic University, Room ZS621, South Wing, Block Z, 181 Chatham Road South, Kowloon, Hong Kong.

Phone: 852-2766-5976; Email: xiaolin.zhu@polyu.edu.hk

30 **Abstract:** Clouds and cloud shadows block land surface information in optical satellite images.
31 Accurate detection of clouds and cloud shadows can help exclude these contaminated pixels in
32 further applications. Existing cloud screening methods are challenged by cloudy regions where
33 most of satellite images are contaminated by clouds. To solve this problem for landscapes where
34 the typical frequency of cloud-free observations of a pixel is too small to use existing methods to
35 mask clouds and shadows, this study presents a new Automatic Time-Series Analysis (ATSA)
36 method to screen clouds and cloud shadows in multi-temporal optical images. ATSA has five main
37 steps: (1) calculate cloud and shadow indices to highlight cloud and cloud shadow information; (2)
38 obtain initial cloud mask by unsupervised classifiers; (3) refine initial cloud mask by analyzing
39 time series of a cloud index; (4) predict the potential shadow mask using geometric relationships;
40 and (5) refine the potential shadow mask by analyzing time series of a shadow index. Compared
41 with existing methods, ATSA needs fewer predefined parameters, does not require a thermal
42 infrared band, and is more suitable for areas with persistent clouds. The performance of ATSA was
43 tested with Landsat-8 OLI images, Landsat-4 MSS images, and Sentinel-2 images in three sites.
44 The results were compared with a popular method, Function of Mask (Fmask), which has been
45 adopted by USGS to produce Landsat cloud masks. These tests show that ATSA and Fmask can
46 get comparable cloud and shadow masks in some of the tested images. However, ATSA can
47 consistently obtain high accuracy in all images, while Fmask has large omission or commission
48 errors in some images. The quantitative accuracy was assessed using manual cloud masks of 15
49 images. The average cloud producer's accuracy of these 15 images is as high as 0.946 and the
50 average shadow producer's accuracy reaches 0.884. Given that it can be applied to old satellite
51 sensors and it is capable for cloudy regions, ATSA is a valuable supplement to the existing cloud
52 screening methods.

53 **Key words:** Cloud detection; Cloud shadow; Mask; Optical satellite images; Time series

54

55 **1. Introduction**

56 Optical satellite images with bands ranging from visible to shortwave infrared are widely
57 used for mapping land cover and land use, monitoring ecosystems, and estimating land surface
58 parameters (Hansen and Loveland, 2012; Zhu and Liu, 2015, 2014). Unfortunately, optical satellite
59 images are easily contaminated by clouds and cloud shadows. This contamination obscures land
60 surface features and alters the reflectance of ground objects, reducing the availability of optical
61 images for applications (Fisher, 2013; Zhu and Woodcock, 2014). Masking clouds and cloud
62 shadows is often the first and a necessary step of image preprocessing in most optical remote
63 sensing applications. Although manual digitization can obtain accurate cloud and shadow masks,
64 it requires a lot of time and effort. Therefore, an automatic method for screening clouds and
65 shadows is needed, especially when processing large numbers of images.

66 Automatic detection of clouds and cloud shadows is challenging (Zhu and Woodcock, 2014).
67 First, different types of clouds have different spectral signatures and are easily confused with some
68 cloud-free bright objects on the land surface, especially in images with limited spectral bands, such
69 as Landsat Multispectral Scanner (MSS) images. The spectral signals of clouds are usually
70 determined by cloud height, optical thickness, particle size, etc. (Platnick et al., 2003). As a result,
71 cloud brightness ranges widely in visible and near infrared bands, and some clouds are easily
72 confused with bright land surfaces, such as concrete surfaces, sand or snow. Second, blurry cloud
73 edges and thin clouds partially obscure land surfaces, making their signal a mixture of cloud and
74 land surface elements and making them difficult to separate from clear observations (Cahalan et
75 al., 2001). Another challenge comes from cloud shadows. They are easily confused with dark land
76 surfaces, such as moist soil, water bodies and topographic shadow (Fisher, 2013).

77 Despite the above challenges, several methods have been developed to automatically screen

78 clouds and cloud shadows in optical images. These methods use one or more of the following rules
79 based on cloud and cloud shadow properties: 1) clouds are generally brighter than ground objects,
80 so they have high reflectance in visible, near and shortwave infrared bands; 2) clouds are generally
81 colder than most ground objects, so they have lower brightness in thermal infrared bands; 3)
82 shadows are generally darker than surrounding land surfaces, so they have lower reflectance in
83 visible, near and shortwave infrared bands; 4) shadows are paired with clouds, so cloud location
84 and solar angles can help locate cloud shadows; and 5) in a sequence of images, pixels affected by
85 clouds and shadows have larger temporal variations than clear observations in the time series. In
86 general, existing methods for masking clouds and cloud shadows can be divided into two
87 categories: single-image methods (Choi and Bindschadler, 2004; Fisher, 2013; Helmer et al., 2012;
88 Huang et al., 2010; Hughes and Hayes, 2014; Irish et al., 2006; Li et al., 2015, 2017; Luo et al.,
89 2008; Martinuzzi et al., 2007; Roy et al., 2010; Scaramuzza et al., 2012; Wilson and Oreopoulos,
90 2013; Zhu and Woodcock, 2012) and multi-temporal or bi-temporal methods (Goodwin et al., 2013;
91 Hagolle et al., 2010; Jin et al., 2013; Wang et al., 1999; Zhu and Woodcock, 2014).

92 Most existing single-image methods use either predefined thresholds or adaptive thresholds
93 to screen clouds in individual images. For example, Luo et al. (2008) identify clouds in MODIS
94 images if pixel reflectance satisfies these predefined thresholds: $(B1 > 0.18 \text{ or } B3 > 0.20)$ and $B6 >$
95 0.16 and $\text{Maximum}(B1, B3) > B6 \times 0.67$, where $B1$, $B3$, and $B6$ are reflectance of MODIS bands
96 1 (blue), 3 (red), and 6 (shortwave infrared), respectively. This MODIS cloud screening method
97 was further adopted for Landsat-8 images (Wilson and Oreopoulos, 2013). Huang et al. (2010) use
98 adaptive thresholds defined in the reflectance-temperature space to mask clouds in Landsat TM
99 and ETM+ images. These adaptive thresholds are defined by the mean and standard deviation of
100 pixel values of individual bands in the whole image. The Automatic cloud cover assessment

101 (ACCA) algorithm consists of twenty-six filters and rules applied to Landsat bands to detect clouds
102 (Irish et al., 2006). ACCA was used to produce web-enable Landsat data (WELD), a consistent,
103 long-term, and large-area data record (Roy et al., 2010). The multi-feature combined (MFC)
104 method uses thresholds in spectral, geometric and texture features to detect clouds in GaoFen-1
105 imagery (Li et al., 2017). Zhu and Woodcock (2012) proposed a method called function of mask
106 (Fmask) for detecting clouds in Landsat TM and ETM+ images. Fmask uses all Landsat image
107 bands and several band indices, such as the normalized difference vegetation index (NDVI) and
108 the normalized difference snow index (NDSI). It employs more than 20 predefined and adaptive
109 thresholds to mask clouds. Besides the above methods using predefined or adaptive thresholds,
110 machine-learning algorithms have been employed to model the complex relationships between
111 image features and clouds using a training dataset. Then, the trained model is used to screen clouds
112 in other images. These machine learning algorithms include decision trees (Scaramuzza et al.,
113 2012), neural networks (Hughes and Hayes, 2014) and support vector machines (Li et al., 2015).
114 Of several tested cloud and shadow masking algorithms that use only a single image, Fmask is
115 globally the most accurate one that requires a thermal band (Foga et al., 2017). Of methods not
116 requiring a thermal band, a version of ACCA (Irish et al., 2006) that uses a simulated thermal band
117 is better overall, but it is not as accurate as Fmask with the thermal band (Foga et al., 2017).
118 Recently, Fmask was further improved for mountainous areas through integrating Digital
119 Elevation Models (DEMs) into the detecting process (Qiu et al., 2017).

120 In these single-image methods, shadow detection is often subsequent to cloud detection. In
121 general, the possible shadow locations can be calculated from the geometric relationship between
122 sun, sensor, and clouds. The calculation requires cloud heights, which can be estimated with
123 brightness temperature derived from thermal infrared bands, because temperature declines with

124 elevation (Qiu et al., 2017; Zhu and Woodcock, 2012). Some methods also use the fact that cloud
125 shadows are dark to confirm whether the possible shadow location estimated from geometry is real
126 cloud shadow, including Fmask (Zhu and Woodcock, 2012) and MFC (Li et al., 2017). In Fmask,
127 predefined thresholds in the near infrared (NIR) band are used to produce a potential shadow mask,
128 which is further compared to the possible shadow locations. If there is a high similarity between
129 potential shadow masks and possible shadow locations, the shadow pixels are finally confirmed
130 (Zhu and Woodcock, 2012).

131 For multi-temporal methods, temporal information in the images acquired at different times
132 is used to detect clouds and shadows. Wang et al. (1999) used the brightness difference between a
133 target image and a reference cloud-free image to detect clouds. Lyapustin et al. (2008) developed
134 an algorithm, abbreviated as MAIAC CM, to detect clouds in time series of MODIS images. The
135 general idea of MAIAC CM is to use the low covariance between reference cloud-free image
136 blocks and cloudy image blocks as a criterion to identify clouds in the time series. Hagolle et al.
137 (2010) computes differences in the blue band between a target image and a cloud-free reference
138 image. It then flags cloud pixels if variations are larger than a threshold. Goodwin et al. (2013)
139 uses filters to smooth the time-series and then identify clouds and shadows based on reflectance
140 differences between each point in the time series and the smoothed time series. Zhu and Woodcock
141 (2014) propose a new algorithm called multiTemporal mask (Tmask) to improve Fmask. Tmask
142 fits a time series model of each pixel using remaining clear pixels based on an initial cloud mask
143 from Fmask. Then, it compares model estimates with observations in the time series to detect cloud
144 and shadow pixels which are omitted in the initial screening by Fmask. In general, these multi-
145 temporal methods are better at detecting clouds and cloud shadows than single-image methods.
146 The temporal information is a valuable complement to the spectral information for differentiating

147 cloud, cloud shadow and clear observations over land surfaces (Goodwin et al., 2013; Zhu and
148 Woodcock, 2014).

149 However, these multi-temporal methods still face challenges in areas with persistent cloud
150 cover, such as tropical and subtropical regions (Ju and Roy, 2008). First, in these areas cloud-free
151 observations may be the exception rather than the rule, making it difficult to know whether the fit
152 of a time series represents clear or cloudy conditions, which limits the application of existing time-
153 series methods (Foga et al., 2017). Example limitations include the requirement by the MAIAC
154 CM method of a cloud free image as a reference image (Lyapustin et al., 2008), and the
155 recommendation for Tmask of 15 cloud-free observations for estimating the time series model
156 (Zhu and Woodcock, 2014). Second, most existing methods were designed for images of a specific
157 sensor, so they lack flexibility. For example, Fmask and Tmask were designed for Landsat TM,
158 ETM+, and OLI images, so they cannot be directly applied to the old Landsat MSS data with
159 limited bands. Third, most of the current methods use predefined fixed thresholds to detect clouds
160 and shadows in an entire scene. For instance, in Tmask, a pixel with observed green band
161 reflectance of 0.04 higher than the time series model estimation will be identified as cloud.
162 Considering the complex situation of clouds and shadows and the diversity of objects on land
163 surfaces and in coastal areas, these fixed thresholds may not always obtain satisfactory results.

164 To overcome the above limitations of existing methods in cloudy regions, the objective of
165 this study is to develop a new automatic method for accurately screening clouds and cloud shadows
166 in multi-temporal optical images in places with persistent clouds. Our scope of inference is
167 landscapes where are so cloudy that the typical frequency of cloud-free observations of a pixel is
168 too small to use existing methods to mask clouds and shadows with image time series. The new
169 method should have the following strengths: 1) it needs fewer predefined parameters; 2) it is

170 suitable for areas with persistent clouds; and 3) it needs a minimal number of bands. Automatic
171 Time-Series Analyses (ATSA) method was developed in this study and tested in three pilot sites
172 using Landsat OLI and MSS images, and Sentinel-2 images. Its performance was compared with
173 Fmask, a widely recognized method.

174 **2. Test Sites and Data**

175 2.1. A cloudy urban site

176 Urban landscapes bring more challenges to automatic screening of clouds and shadows than
177 other landscapes. The bright built-up area often leads to large commission errors in cloud detection.
178 To test the effectiveness of the proposed method in such challenging cases, we selected Hong Kong,
179 a cloudy subtropical dense city with complex and mixed land-cover types (Fig. 1). This site has an
180 area of 1, 620 km² (1200×1500 Landsat pixels), and the central coordinates are 22.367° N and
181 114.123° E. It is covered by the Landsat scene of Worldwide Reference System 2 (WRS-2) Path
182 122 Row 44. All 23 available Landsat-8 OLI level-1 images in 2015 were downloaded from USGS
183 Earth Explorer. These images were then converted to Top of Atmosphere (TOA) reflectance with
184 the scaling coefficients in the metadata file. The corresponding Fmask cloud masks of these images
185 were also downloaded from USGS Earth Explorer. Based on Fmask cloud masks, only two images
186 are clear, while the other images have total cloud and shadow coverage ranging from 5.5% to 97%.
187 Sixteen of them have total cloud and shadow coverage larger than 60%, indicating Landsat
188 imagery in this site is seriously contaminated by clouds (Table 1).

189



190

191

Fig. 1. True color composition of a Landsat-8 image of 2015, DOY003 in Hong Kong

192

193

194

195

196

197

198

199

200

201

202

203

Table 1. Summary of cloud and shadow coverage of Landsat-8 images from the year 2015 over

204

the Hong Kong site using Fmask product. Only two images have no clouds.

DOY	Cloud coverage %	Shadow coverage %	Total cloud and shadow coverage%
3	0.0	0.0	0.0
19	0.0	0.0	0.0
35	97	0.0	97
51	65	3.8	69
67	90	0.65	90
83	87	3.1	90
99	89	0.0	89
115	82	0.06	82
131	32	5.4	38
147	94	0.25	94
163	64	3.7	68
179	62	10	72
195	48	6.8	55
211	83	2.7	85
227	95	0.00	95
243	95	0.36	95
259	93	0.52	93
275	78	4.2	82
291	6.6	2.2	8.7
307	93	0.71	93
323	42	12	55
339	3.7	1.8	5.5
355	79	14	93

205

206 2.2. A cloudy forest site

207 Dense time series data are needed for monitoring vegetation dynamics, and monitoring
208 tropical and subtropical forests is very important to quantifying their important role in the global
209 carbon cycle. However, persistent cloud cover poses challenges when monitoring tropical forest
210 vegetation. To investigate the accuracy of the proposed method to screen clouds and shadows in
211 cloudy tropical forest regions, the second site is northeastern Puerto Rico (Fig. 2). This site has an
212 area of 1,836 km² (1200×1700 Landsat pixels), and the central coordinates are 18.321° N and
213 65.838° W. The major land cover type is forest, including the El Yunque National Forest, where
214 extensive tropical montane cloud forests occur that by definition are persistently cloudy. This site

215 also includes bright, wet and dark features that are easily confused with clouds or cloud shadows.
216 It includes much of the capital city of Puerto Rico, San Juan, coastal areas with features like sand,
217 rock and coral reefs, topographic shadow associated with steep topography and many fields with
218 bright, wet or bare soils. The Landsat WRS-2 scene Path 4 and Row 47 covers the area. A total of
219 18 Landsat 8 OLI images from May 26 2013 to May 29 2014 (i.e., one-year length) and their
220 corresponding Fmask cloud layers were downloaded from USGS Earth Explorer. The total cloud
221 and shadow coverage of the images as estimated by Fmask ranges from 5% to 81%, and the mean
222 coverage is 45%, indicating this site is also seriously affected by clouds. In this site, another 11
223 Landsat-4 MSS images from the year 1983 were collected to test the performance of the proposed
224 method for screening clouds and shadows in images with limited bands and low radiometric
225 resolution. For these MSS images, corresponding Fmask cloud masks are not available from USGS
226 Earth Explorer because Fmask uses thermal bands, which are not included in MSS images.
227 Through visual inspection, these 11 MSS images have diverse cloud and shadow coverage, from
228 almost cloud-free to fully covered by clouds.



229

230 Fig. 2. True color composition of a Landsat-8 image from 2013 (DOY210) of northeastern
231 Puerto Rico.

232
233
234

Table 2. Summary of cloud and shadow coverage of Landsat 8 OLI images for the Puerto Rico site using Fmask product

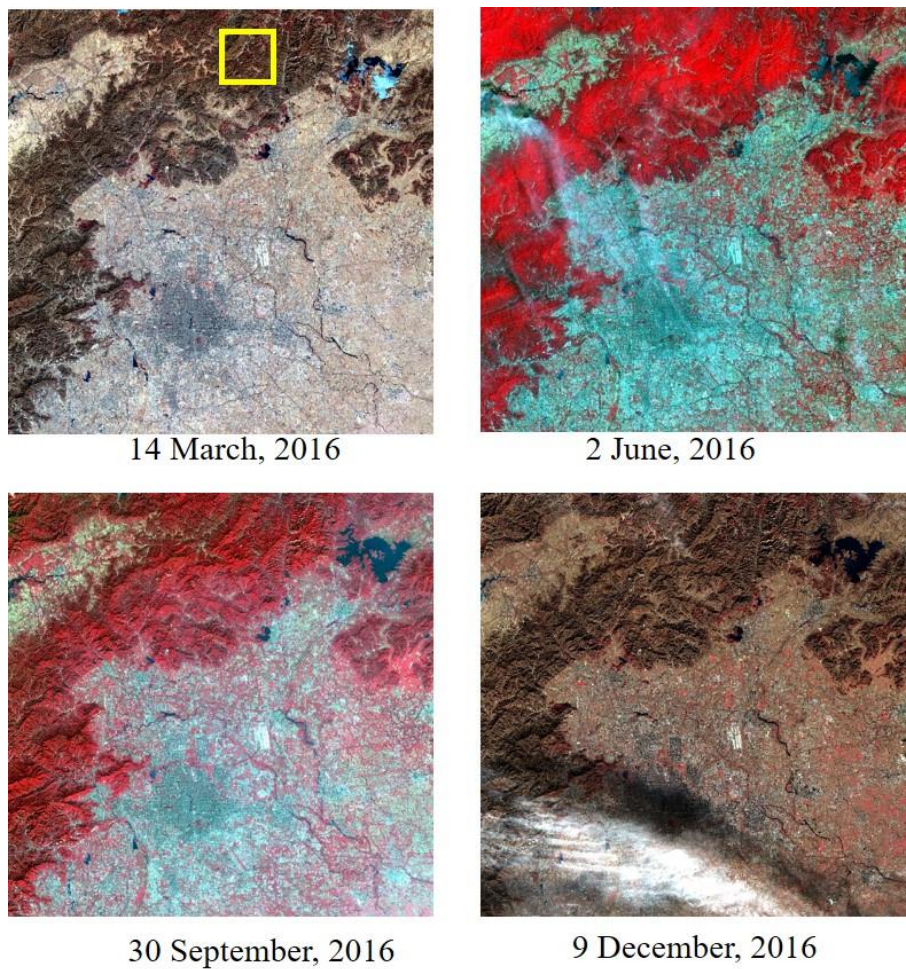
DOY	Cloud coverage %	Shadow coverage %	Total cloud and shadow coverage%
146	41	4.1	45
178	43	8.0	51
210	4.3	1.6	5.9
226	39	5.6	45
242	40	8.2	48
258	28	6.5	35
274	67	14	81
290	27	8.1	35
306	8.5	1.1	9.6
322	30	6.7	37
354	58	13	71
5	24	11	35
21	43	13	56
53	41	12	54
69	31	9.5	41
117	37	6.5	44
133	38	3.0	41
149	59	14	72

235

236 2.3. A seasonal-change site

237 Strong seasonality is another challenge for most multi-temporal cloud screening methods.
238 The large variation of spectral values due to seasonality may be confused with the variation due to
239 occurrence of clouds and cloud shadows. To investigate the accuracy of the proposed method to
240 screen clouds and shadows in regions with strong seasonality, the third site is Beijing metropolis
241 and its surrounding rural areas (Fig. 3). This site is covered by an entire Sentinel-2 tile (about
242 12,000 km²), and the central coordinates are 40.154° N and 116.495° E. This site has a lot of bright
243 land surface and its vegetation is deciduous with strong seasonality. Images from different seasons
244 in Fig. 3 show that vegetation grows to a peak greenness in summer and loses leaves in winter. In
245 addition, the high mountains in this site bring difficulties for both cloud and cloud shadow

246 detection. Twenty Sentinel-2 images in 2016 with varying cloud cover were downloaded from
247 USGS Earth Explorer (Table 3). The Fmask cloud masks of these Sentinel-2 images were obtained
248 using the Matlab code (Version 3.3; <https://github.com/prs021/fmask>) specific for Sentinel-2
249 images (Zhu et al., 2015). The total cloud and shadow coverage of the images as estimated by
250 Fmask ranges from 0.1% to 100%, and 7 images have less than 20%, indicating this site has more
251 clear images than the other two sites.



252
253 Fig. 3. False-color Sentinel-2 images in Beijing from different seasons in 2016 (the yellow box
254 in upper left image is a forest region of interest (ROI) used to demonstrate the seasonality in Fig.
255 9)
256
257

258

259
260
261
262
263
264
265
266

Table 3. Summary of cloud and shadow coverage of 20 Sentinel-2 images in 2016 for the Beijing site using cloud masks by Fmask

Date	Cloud coverage %	Shadow coverage %	Total cloud and shadow coverage%
Jan.26	42.4	17.7	60.1
Mar.14	0.7	0.5	1.2
Mar.24	0.1	0.0	0.1
Apr.3	0.2	0.2	0.4
Jun.2	13.2	1.8	15.0
Jun.12	56.4	6.2	62.6
Jul.22	90.3	9.7	100.0
Aug.1	78.6	4.6	83.2
Aug.11	41.2	9.4	50.6
Aug.21	22.6	6.1	28.7
Aug.31	7.6	4.6	12.2
Sep.20	36.4	3.5	39.9
Sep.30	34.4	8.1	42.5
Oct.10	19.3	7.3	26.6
Oct.20	100.0	0.0	100.0
Oct.30	75.7	9.3	85.0
Nov.19	2.6	1.8	4.4
Nov.29	100.0	0.0	100.0
Dec.9	16.0	8.8	24.8
Dec.29	7.1	4.1	11.2

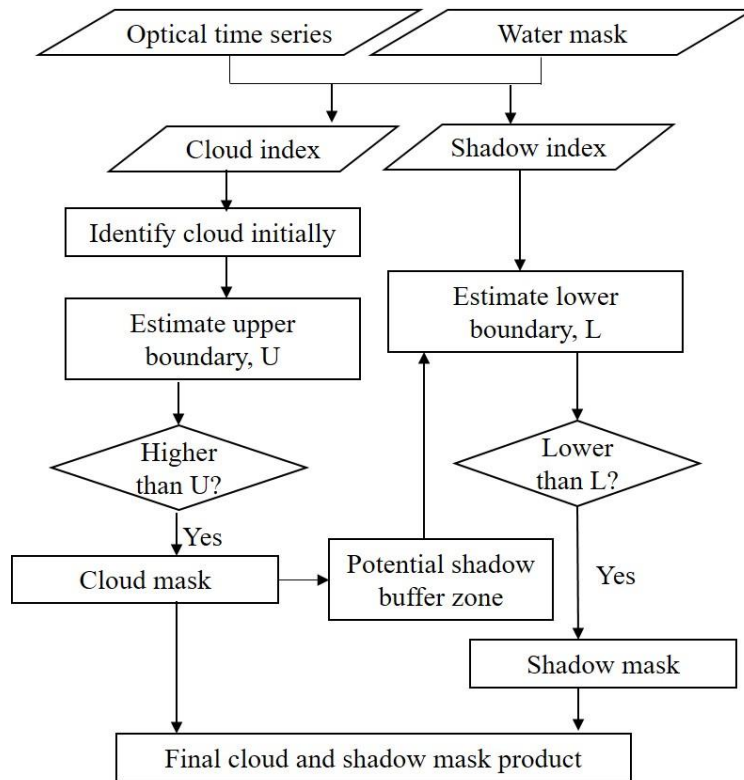
267

268 **3. Methodology**

269 There are five main steps in ATSA (Fig. 4). Either TOA reflectance or surface reflectance data
270 can be used as inputs. The five main steps are: (1) compute a cloud index and a shadow index from
271 the image bands to highlight cloud and shadow pixels; (2) detect clouds initially with unsupervised

272 clustering of these indices for individual images in the time series; (3) refine the cloud pixels
 273 through analyzing the time series of the cloud index; (4) predict the potential shadow locations
 274 through the geometric relationships among the sun, clouds, and the Earth surface; (5) confirm the
 275 real shadow pixels through analyzing the time series of the shadow index. We detail these steps
 276 below.

277



278

279 Fig. 4. Flowchart for the Automatic Time-Series Analysis (ATSA) to screen clouds and cloud

280 shadows

281

282 3.1. Calculate cloud index and shadow index

283 Given the wide ranges of reflectance values exhibited by diverse cloud- and Earth surface
 284 types, individual spectral bands from one image cannot accurately differentiate clouds, cloud

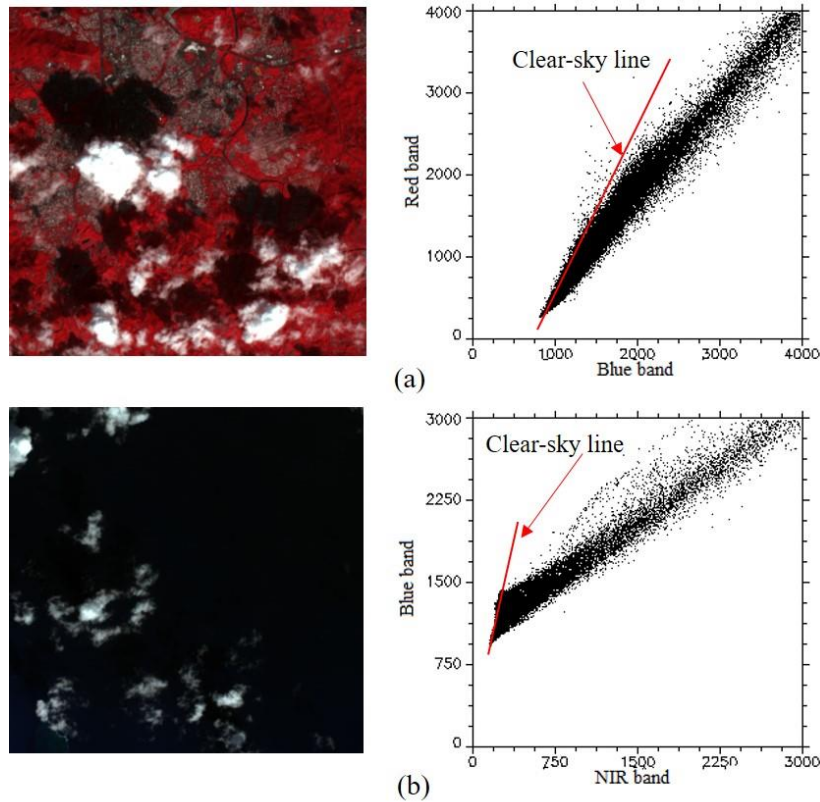
285 shadows and clear observations. With image time series, significant seasonality of some land cover
286 types (*e.g.*, natural vegetation and agriculture) and land-cover change (*e.g.*, deforestation and
287 urbanization) lead to large temporal variability of reflectance in image time series, which is easily
288 confused with temporal variability caused by clouds and cloud shadows. Therefore, there is a need
289 to combine or transform individual bands to get indices that highlight the clouds and cloud
290 shadows while compressing variability in other land cover types, so that clear observations have
291 values that are as stable as possible in the time series.

292 As land and water surfaces have very different spectral characteristics (Zhu and Woodcock,
293 2012), the cloud and shadow indices are designed separately for land and water surfaces. A water
294 mask is needed in our method. Fortunately, a water mask can be easily obtained through classifying
295 a cloud-free image in the time series or from an existing water mask. There are now several water
296 masks available at different resolutions, such as a 30-m water mask from a Landsat-based global
297 land cover product (Chen et al., 2015) and a 250-m global water mask from MODIS data (available
298 in <http://landcover.org/data/watermask/>). In our test experiments, we classified a cloud-free image
299 to obtain the water mask.

300 For land surfaces, we used the haze optimal transformation (HOT) as a cloud index. The HOT
301 transformation is derived from an analysis of Red-Blue spectral space. These two bands have a
302 perfect linear relationship for diverse land cover types under clear-sky conditions (Zhang et al.,
303 2002), and Zhang et al. (2002) name this perfect line the clear-sky line (see the red line in Fig. 5
304 a). For pixels contaminated by haze and clouds, their spectral response in Red-Blue space is very
305 different from the clear-sky line, so the HOT index was designed to quantify the perpendicular
306 distance of a pixel from the clear-sky line:

$$HOT = \frac{|a \times B_{Blue} - B_{Red} + b|}{\sqrt{1 + a^2}} \quad (1)$$

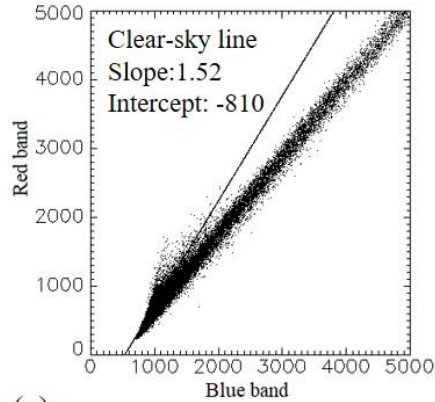
307 where B_{Blue} and B_{Red} are pixel values of blue and red bands respectively, and a and b are the slope
 308 and intercept of the clear-sky line.



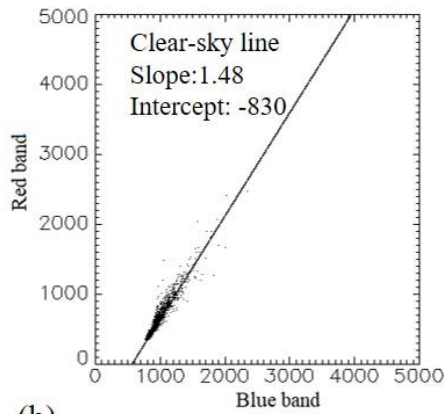
309
 310 Fig. 5. A land-surface subset of a Landsat-8 image and its Red-Blue scatter plot (a) and a water-
 311 surface subset Landsat-8 image and its NIR-Blue scatter plot (b)

312
 313 In the original HOT transformation (Zhang et al., 2002), the clear-sky line comes from
 314 regressing spectral values of pixels selected from areas of a scene that visually are deemed to be
 315 the clearest. To make our method automatic, we employed a bin-based approach to search for the
 316 clearest pixels in each scene. This approach has three steps: (1) divide the 0-0.15 range of blue

317 reflectance values into 50 bins with equal intervals, because cloud-free pixel values of most land-
318 cover types are within this range; (2) for each bin, select the 20 pixels with the largest reflectance
319 values in the Red band and compute the average value of these selected pixels for red and blue
320 bands, respectively, yielding a pair of red and blue reflectance values for each bin (B_{Redi} , B_{Bluei}) ;
321 (3) for all 50 pairs of (B_{Redi} , B_{Bluei}), regress B_{Redi} against B_{Bluei} to get the clear-sky line using the
322 least absolute deviation (LAD) regression method to avoid the effect of outliers (Bassett and
323 Koenker, 1978). If some images in the time series are completely covered by clouds, no clear
324 pixels can be found for estimating the clear-sky line. For these completely cloud-covered images,
325 the average slope and intercept of clear-sky lines derived from other images in the time series are
326 used to compute the HOT index. To demonstrate the effectiveness of a bin-based automatic
327 approach, the retrieved clear-sky line in a sub-image was compared with the result using manually
328 selected clear pixels (Fig. 6). The slope and intercept of the clear-sky line from the bin-based
329 approach is very similar to the results from the manual approach.



(a)



(b)

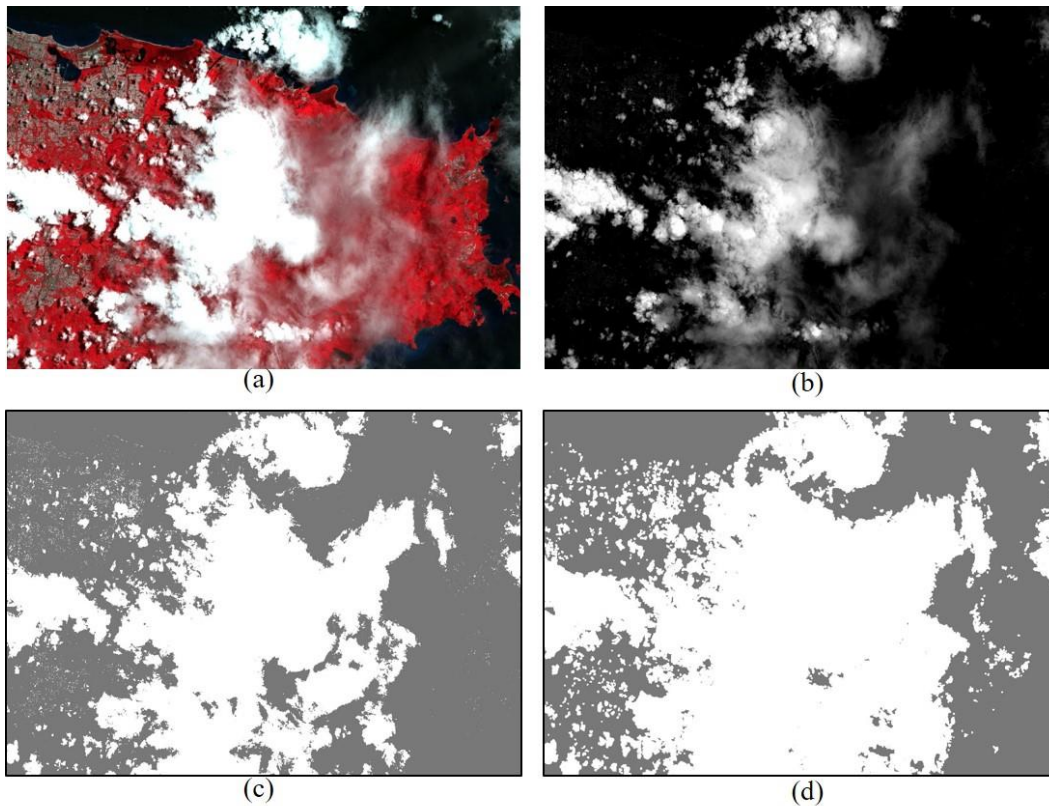
330
331 Fig. 6. Comparison between the clear-sky line of a sub-image estimated by the proposed
332 automatic bin-based approach (a) and that using manually selected clear pixels marked by red
333 ROIs (b).

334

335 For water surfaces, the cloud-free pixel values of the red and blue bands are not on the clear-
336 sky line, leading to large HOT values that are confused with thin clouds. Consequently, a new HOT
337 index, designed specifically for water surfaces, is needed. In the Blue-NIR space, the spectral
338 response of cloud-free water pixels, including turbid or shallow water and coral reefs, is very
339 different from cloudy pixels (Fig. 5b). A new HOT index for water surface, HOT_w is given as:

$$HOT_w = \frac{|a_w \times B_{NIR} - B_{Blue} + b_w|}{\sqrt{1 + a_w^2}} \quad (2)$$

340 where a_w and b_w are the slope and intercept of the clear-sky line for water bodies and are obtained
 341 through the same method as for the land surface. Then, the HOT indices for land and water surfaces
 342 are combined to yield a cloud index map (Fig. 7b). In this cloud index map, we can see that the
 343 HOT transformation yields an index with a larger difference between cloud and bright non-cloud
 344 objects than the individual visible bands. All clouds and haze are highlighted by larger values (i.e.
 345 white color) while all cloud-free pixels have a very low value (i.e. dark color).



346
 347 Fig. 7. False color Landsat-8 image of DOY149 in the Puerto Rico site (a), its corresponding
 348 HOT cloud index (b), initial cloud mask (c), and final cloud mask (d). In (c) and (d): gray is clear
 349 pixels and white is clouds. The time series analysis adds thin clouds to the initial cloud mask,
 350 and the minority analysis removes scattered bright pixels in urban and coastal areas in the upper

351 left of panel (c), which would otherwise be confused with clouds.

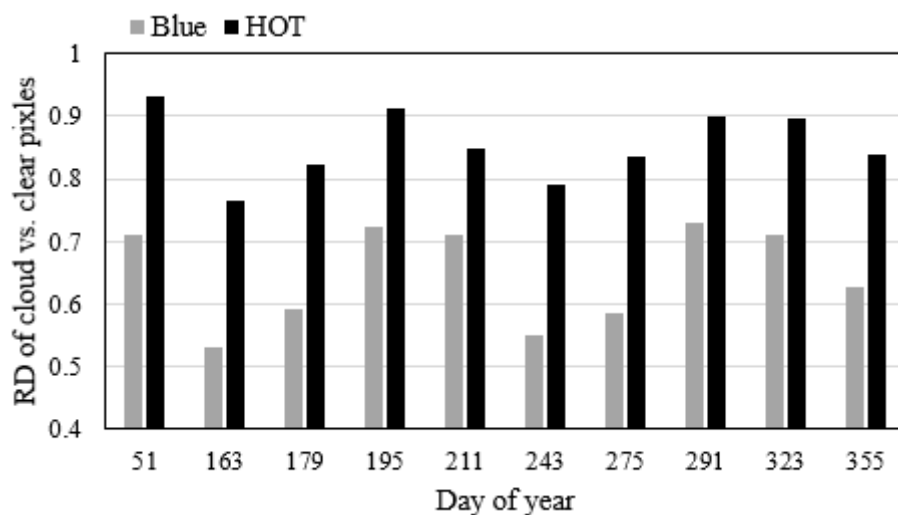
352

353 To further compare the ability of the original bands and HOT for discriminating clouds and
354 clear land surface, the relative difference (RD) between cloud and cloud-free pixels in each image
355 was computed:

$$RD = \frac{\bar{B}_{cloud} - \bar{B}_{clear}}{\bar{B}_{cloud}} \quad (3)$$

356 where \bar{B}_{cloud} and \bar{B}_{clear} are average values of cloudy pixels and clear pixels respectively. RD
357 ranges from 0 to 1 and larger values indicate a higher separability between cloudy and clear pixels.

358 Fig. 8 shows the RD values of the Blue band and the HOT index of Landsat-8 images which contain
359 both clear and cloudy pixels in the Hong Kong site. Hong Kong includes both forests and
360 considerable bright urban surfaces. It is a challenging site for cloud detection. We can see that in
361 these images HOT index is better than the original Blue band at separating clouds from clear land
362 surfaces. The comparisons of RD values between the Red band and the HOT index, and between
363 the NIR band and the HOT index, have a similar pattern (results not shown).



364 Fig. 8. Relative difference (RD) between the average value of cloudy and clear pixels of the Blue
365

366 band and the HOT index in Hong Kong Landsat-8 images. A larger RD indicates higher
367 separability between cloud and clear pixels.

368

369 For cloud shadows, direct solar radiation is blocked by clouds, so the shadow pixels are
370 illuminated by scattered light. Because the atmospheric scattering is weaker at longer wavelengths,
371 the NIR and SWIR bands of shadow pixels are much darker than surrounding clear pixels (Zhu et
372 al., 2015). Therefore, the shadow index (SI) is defined as:

$$SI = B_{NIR} + B_{SWIR} \quad (4)$$

373 However, water also absorbs most radiation at longer wavelengths, so water pixels not
374 obstructed by clouds are as dark as shadow pixels in NIR and SWIR bands (Li et al., 2017).
375 Consequently, for water surfaces, the shadow index is calculated with the blue and green bands:

$$SI_w = B_{Blue} + B_{Green} \quad (5)$$

376 For old satellite images with fewer bands, such as Landsat MSS images with only green, red,
377 and 2 NIR bands, the green band replaces the blue band in Eqs. (1, 2, and 5), because it is highly
378 correlated with blue band. Also, the second NIR band replaces the SWIR band in Eq. (4), because
379 both the NIR and SWIR bands are good indicators of cloud shadows. Similarly, for other sensors
380 without SWIR bands, such as IKONOS, we anticipate that only one NIR band would be used as
381 the shadow index for land surfaces.

382

383 3.2. Detect cloud initially

384 All cloud index images of the time-series are classified by an unsupervised classifier, k-means,
385 to get the initial cloud mask. First, a certain number (e.g. 10,000) of sample pixels are selected by
386 systematic sampling of all cloud index images. Selecting samples from all images in the time series

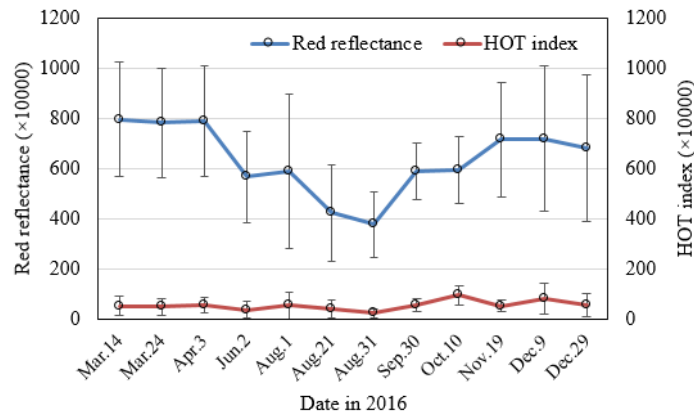
387 ensures that samples of clear surfaces, thin clouds, and thick clouds are included. Using the
388 selected samples rather than all pixels speeds up the k-means optimization in the next step. Second,
389 these samples are classified with the k-means method into three classes. The three classes are
390 labeled based on the relative value of the class means, i.e., the lowest class mean is clear pixels,
391 the middle one is thin clouds, and the highest one is the thick clouds. The k-means method uses an
392 iterative procedure. At each iteration, each sample is assigned to one class based on the closeness
393 to the class means obtained from the last iteration, and new class means are updated using new
394 class labels of samples. The iterative process will be ended when the class labels no longer change
395 (Lloyd, 1982). Third, individual pixels in each cloud index image of the time series are identified
396 as thin clouds, thick clouds, or cloud-free observations based on which class has the smallest the
397 cloud-index distance from the class means of the sample pixels. Finally, an initial cloud mask is
398 produced for each image by combining thin clouds with thick clouds (Fig. 7c). The ranges of cloud
399 index values for the three classes (thin clouds, thick clouds and clear), being derived from all pixels
400 in the time series, form a set of thresholds that are adapted to a time series rather than a single
401 image.

402

403 3.3. Detect remaining extremely thin clouds and remove bright pixels that are not cloud or haze

404 Although the initial cloud mask already identifies most cloudy pixels, it may omit some
405 cloudy pixels, especially extremely thin clouds and cloud edges with lower values of the cloud
406 index. Therefore, the initial cloud masks need to be further improved with temporal information.
407 For each pixel, its time series may include both cloudy points and cloud-free observations. In
408 general, cloudy points have larger variations in spectral values than clear observations. This
409 temporal property can help to identify cloudy points (Zhu and Woodcock, 2014). However, due to

410 changes in vegetation phenology or land cover, clear observations of some pixels also undergo
 411 temporal variations. However, compared with the original spectral bands, the cloud index derived
 412 from the HOT transformation depresses the temporal variations from different vegetation growth
 413 stages, soil inundation, or land-cover change. For instance, in a forest ROI from the Beijing site
 414 (marked by a yellow box in Fig. 3), the time series of the Red band shows a stronger seasonality
 415 than the HOT index (Fig. 9). The Red band is used to compute the HOT index. It has lower values
 416 in summer due to more absorption by vegetation. In contrast, the HOT index is more stable across
 417 different seasons and with smaller variability than the original Red bands.



418 Fig. 9. Red reflectance and HOT index of cloud-free pixels in a forest ROI in Beijing (marked by
 419 a yellow box in Fig. 3) across different seasons. The circles are mean values and error bars are \pm
 420 1 standard deviation.
 421

422
 423 Therefore, an analysis of the cloud index time series is conducted to refine the initial cloud
 424 mask. Fig. 10 gives an example of a cloud index time series of a pixel from the Puerto Rico site
 425 (column1173, row 1092). There are two points identified as clouds in the initial mask (the red
 426 points). Most of the other points (the black ones) should be clear observations. They are used to
 427 find an upper boundary in the HOT index for clear pixels, $U(i)$. Points above this threshold are
 428 then also designated as cloudy. For i th pixel:

$$U(i) = \text{mean}\{HOT(i, t)|(i, t) \notin \mathbf{C}\} + A \times \text{sd}\{HOT(i, t)|(i, t) \notin \mathbf{C}\} \quad (6)$$

429 where $\text{sd}\{\cdot\}$ is the standard deviation of the HOT index through the time series, $HOT(i, t)$ is the
 430 HOT index value of the i th pixel at time t , and \mathbf{C} is the set of cloudy points from the initial masks
 431 for i th pixel. A is a standard deviation multiplier that defines the upper boundary. A can be assigned
 432 a recommended value from 1 to 2. Smaller values would be able to identify thinner clouds, but
 433 meanwhile increase the risk of commission errors, *i.e.*, identifying “clear” observations as cloudy
 434 points. In existing methods, this parameter is a constant for all pixels in the image (Goodwin et al.,
 435 2013; Hagolle et al., 2010). However, cloud frequency is different in different parts of the image,
 436 so some pixels may include more cloud points in the HOT time series that are omitted in the initial
 437 detection than others. Therefore, we need to consider this difference among pixels when we set the
 438 value of parameter A . In general, clouds cause large variations in the HOT time series. We
 439 introduced a new variable, the normalized difference range index (NDRI), to tune the parameter
 440 A :

$$NDRI(i) = (T_{kmeans} - Range_i)/(T_{kmeans} + Range_i) \quad (7)$$

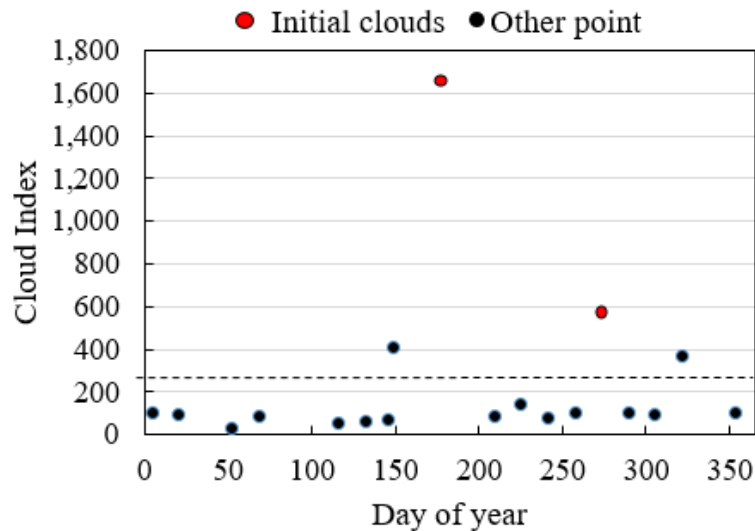
$$Range_i = \max\{HOT(i, t)|(i, t) \notin \mathbf{C}\} - \min\{HOT(i, t)|(i, t) \notin \mathbf{C}\} \quad (8)$$

441 where T_{kmeans} is the minimum HOT value of all cloud pixels identified by K -means in section 3.2.
 442 $NDRI$ is further used to adjust the parameter A in Eq. (6) as a pixel-wise parameter $A(i)$:

$$A(i) = A + NDRI(i) \quad (9)$$

443 The value for $A(i)$ is used in Eq. (6) to calculate the pixel-level upper boundary U for each pixel
 444 in the time series. $A(i)$ further tunes the pixel-level upper boundary U by adapting the standard
 445 deviation multiplier to the temporal variability of each pixel. Because $NDRI$ is added to A , we
 446 recommend an A value from 0.5 to 1.5 (instead of 1 to 2). Pixels with larger variation in the HOT

447 time series will have a lower upper boundary, i.e. a stricter threshold. Any points above the upper
448 boundary, e.g. the dashed line in Fig. 10, will be identified as clouds.



449
450 Fig. 10. An example of cloud index time series: the two black points above the dashed line are
451 identified as clouds based on the time series analysis.

452 The cloudy points detected from the time series analysis are the final cloud mask (Fig. 7d).
453 This step adds more thin clouds to the initial mask and also contributes to filtering bright non-
454 cloud objects. For instance, very bright land surfaces (e.g., airport runways and beach sand) may
455 show consistently high values in the cloud-index time series, leading to a high threshold in Eq. (6).
456 As a result, pixels of these bright land surfaces are not likely to be identified as clouds because
457 their cloud index values are unlikely to exceed the high threshold. In addition, assuming that clouds
458 are generally wider than a few pixels at Landsat spatial resolution, isolated pixels identified as
459 being cloudy are removed from the cloud mask using a repeated minority analysis. We removed
460 cloud pixels if 4 or fewer pixels in the 3-by-3 neighborhood of a pixel are cloud pixels. This step
461 removes any remaining isolated, bright pixels in urban and coastal areas that are not clouds. Finally,
462 similar to Fmask, all cloud patches are buffered with a width of 1 pixel to further reduce omission
463 errors around cloud edges.

464

465 3.4. Estimate potential shadow zones

466 Shadow pixels are easily confused with dark objects and topographic shadow even in shadow
467 index maps. However, clouds always accompany cloud shadows except at scene edges. This
468 characteristic can help reduce commission (e.g., wet soil, topographic shadow) errors of cloud
469 shadow detection. Actually, the location of cloud shadows can be calculated by the precise
470 geometric relationship among clouds, cloud shadows and the position of the sun (Zhu and
471 Woodcock, 2012). For a cloudy pixel with coordinates (x, y) , the location of its corresponding
472 shadow pixel (x', y') can be calculated using following equations (Luo et al., 2008):

$$x' = x - H \times \tan \theta \sin \phi \quad (10)$$

$$y' = y - H \times \tan \theta \cos \phi \quad (11)$$

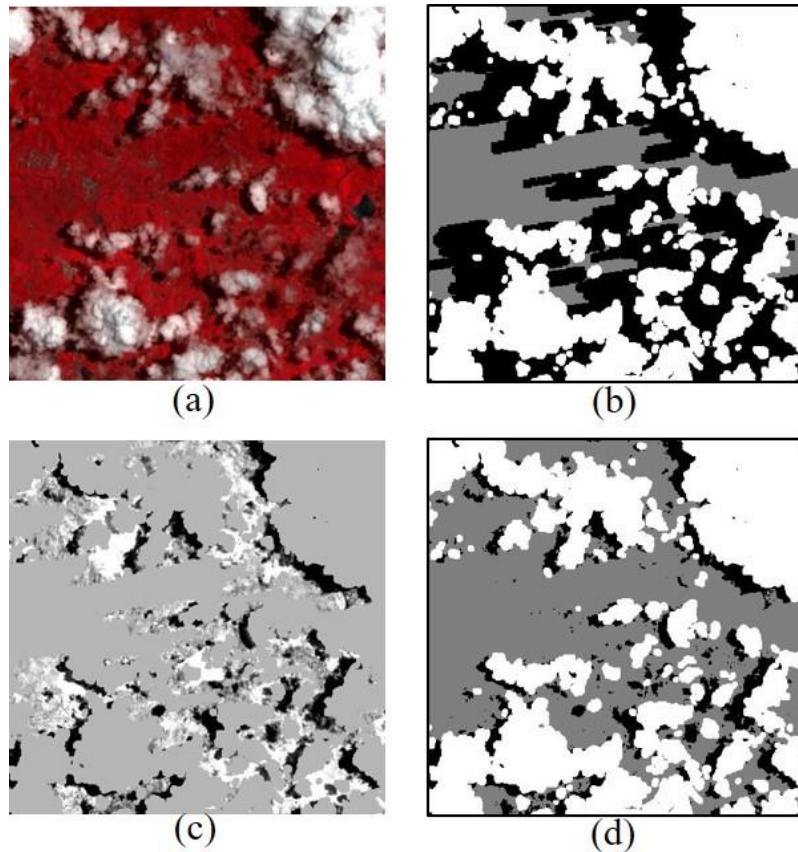
473 where H is the height of clouds above the land surface, and θ and ϕ are solar zenith and azimuth
474 angles. Values of θ and ϕ can be extracted from the image metadata files, but H is unknown for
475 each cloud patch. In most existing methods, the brightness temperature (BT), derived from thermal
476 infrared bands, is used to estimate cloud height with lapse rates for air temperature, such as -
477 9.8K/Km for dry air and -6.5K/Km for moist air (Goodwin et al., 2013; Huang et al., 2010; Zhu
478 and Woodcock, 2012). However, there are two problems with estimating cloud height when
479 locating cloud shadows: (1) the lapse rate varies in different atmospheric conditions, and the BT
480 of thin clouds is also influenced by the land surface; (2) some sensors, especially old ones, do not
481 have thermal infrared bands, such as the Landsat MSS sensor, the CBERS IRMSS sensor and the
482 Sentinel MSI sensors. For Landsat 8 also, a method for masking clouds and shadows that does not
483 require a thermal band is needed. The Thermal Infrared Sensor (TIRS) has some error and
484 intermittent availability and has a shorter design life than the multispectral Operational Land

485 Imager (OLI). That thermal data may not always be available is one obstacle to improving Landsat
486 8 cloud and shadow masks with image time series (Foga et al., 2017; Scaramuzza et al., 2012).

487 To make the proposed method able to process historical images without thermal infrared
488 bands, a range of possible cloud heights are used to estimate all possible shadow locations of a
489 cloud. We can use a default value of 200 m for minimum cloud heights because it is suitable for
490 most areas (Zhu and Woodcock, 2012). The maximum cloud heights can be determined empirically
491 by visually checking the maximum horizontal distance (D_{max}) between clouds and their shadows,
492 or using 12 km based on previous studies (Fisher, 2013; Luo et al., 2008) :

$$H_{max} = \frac{D_{max}}{\sqrt{(\tan \theta \sin \phi)^2 + (\tan \theta \cos \phi)^2}} \quad (12)$$

493 Fig. 11b shows an example of potential shadow zones of a subset of image DOY146 in the
494 Puerto Rico site. We can see that the real shadows are located within the potential shadow zones.
495



496

497 Fig. 11. A subset of the Landsat-8 image DOY146 in the Puerto Rico site (a), its potential shadow
 498 zones (b), shadow darkness as estimated by Inverse Distance Weighting (IDW) (c), and the initial
 499 shadow detected by K-means (d).

500

501 3.5. Detect shadow within potential shadow zones

502 The potential shadow zones mark the possible locations of cloud shadows. They overestimate
 503 the real shadow areas. Therefore, all the pixels within the shadow zones need to be further
 504 confirmed as to whether they are real shadow pixels. In the shadow index images, shadows are
 505 located at places with regional minima (i.e. “holes”) due to their being relatively dark in optical
 506 bands. Some existing methods use flood-fill transformation to predict the image without shadows
 507 and compare it with real images to identify shadow pixels (Li et al., 2017; Zhu and Woodcock,

508 2012). However, this approach may often mislabel dark objects, such as water, as cloud shadow
509 (Li et al., 2017). Here, a similar idea is employed, but the new strategy reduces errors as compared
510 with the flood-fill method. First, in the shadow index images, pixels in potential shadow zones are
511 predicted from surrounding clear pixels with an inverse distance weighted (IDW) interpolator.
512 Second, for those pixels in potential shadow zones, we estimate their “darkness” as their original
513 shadow index minus the predicted values (Fig. 11c, a darker color means higher darkness). This
514 darkness only shows how cloud shadows lower the pixel brightness compared with surrounding
515 clear pixels. Third, similar to initial cloud detection, K-means clustering is applied to these
516 darkened pixels (i.e. pixels with negative darkness values) to classify these pixels into two classes,
517 clear observation and cloud shadow, to yield an initial shadow mask (Fig. 11d).

518 After the initial shadow detection, we apply a time series analysis, similar to the cloudy point
519 refinement, to refine the initial shadow mask. This process aims to reduce both omission and
520 commission errors in the initial shadow mask. Because cloud shadows have darkening effects,
521 which lead to lower shadow index values in the time series of a pixel, a lower boundary L is used
522 as a threshold to identify real shadow points. Considering differences in earth-sun-sensor geometry,
523 atmospheric conditions and vegetation phenology, the shadow index of land surfaces needs to be
524 normalized to minimize these differences prior to the time series analysis. Here, the histogram
525 matching method is used given its simplicity (Helmer and Ruefenacht, 2005). Although histogram
526 matching is a linear correction, and changes in vegetation phenology across an image can be
527 nonlinear (Helmer and Ruefenacht, 2007), we found that histogram matching worked well for
528 mitigating the temporal variability in shadow-index time series. First, the image with the fewest
529 clouds in the time series is selected as a base image. Then, the shadow index of other images is
530 normalized to this base image using the gain and bias:

$$gain = \frac{\sigma_B}{\sigma_t} \quad (13)$$

$$bias = \mu_B - \mu_t \times gain$$

531 where μ_B and μ_t are the mean value of clear pixels in the base image and the image at time t
 532 respectively, σ_B and σ_t are the standard deviations of clear pixels in the base image and the image
 533 at time t respectively. The normalized shadow index value of image at time t , $SI_N(i, t)$, can be
 534 computed as:

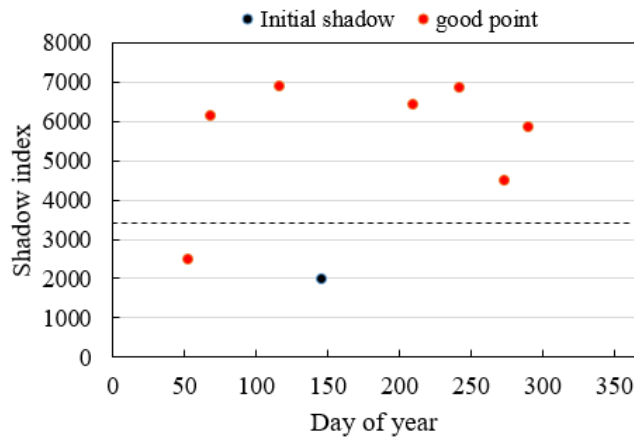
$$SI_N(i, t) = SI(i, t) \times gain + bias \quad (14)$$

535 This lower boundary L is defined using “good” points, which are those points not identified as
 536 shadow in the initial shadow mask (Fig. 12):

$$L(i) = \text{mean}\{SI_N(i, t) | (i, t) \in \text{"good"}\} - B \times \text{sd}\{SI_N(i, t) | (i, t) \in \text{"good"}\} \quad (15)$$

537 where B is a standard deviation multiplier that serves as a parameter to tune the threshold, $L(i)$ is
 538 the lower threshold for pixel i , *mean* is the mean shadow index (SI) of pixel i for the time series,
 539 and *sd* is the standard deviation of the SI for the time series of pixel i . Pixels with SI brighter than
 540 $L(i)$ are deemed too bright to be cloud shadow. The recommended value of B is from 1 to 3, and a
 541 larger value will select *darker* shadows, *i.e.*, it will darken the threshold for designating whether
 542 pixels are shadow. Therefore, the parameter B should be set to balance the omission and
 543 commission errors for shadow detection. For the initial shadow points, they are confirmed as real
 544 shadow if their shadow index values are lower than the mean value of “good” points. This step
 545 reduces the commission errors in initial shadow detection. For other points in the time series which
 546 are marked as potential shadow using sun-cloud geometry, they will be identified as final shadow
 547 points if their shadow index values are lower than L (Fig. 12). This step reduces the omission errors

548 in the initial shadow detection. It should be noted that although the potential shadow zones and
549 time series analysis can greatly prevent classifying topographic shadow as cloud shadow,
550 topographic shadow within the potential shadow zones may be identified as cloud shadows if it is
551 as dark as cloud shadow.



552
553 Fig. 12. An example of shadow index time series analysis: the points below the dashed line are
554 identified as cloud shadow. The dashed line represents L , the lower threshold.

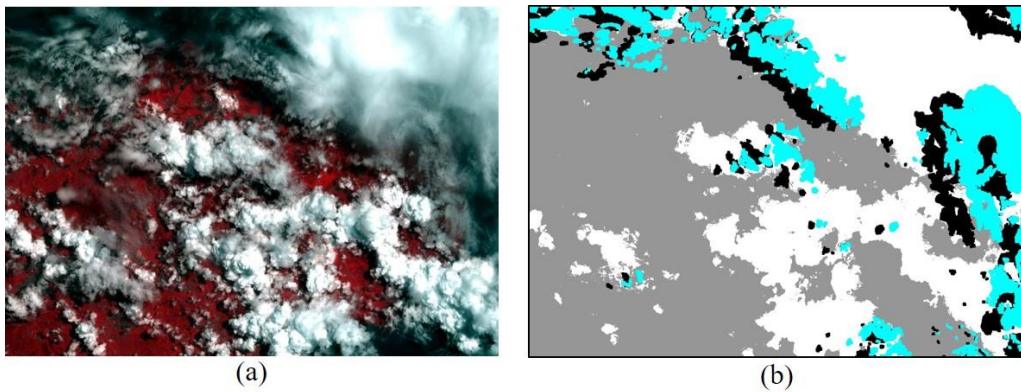
555
556 Similar to the cloud mask, isolated shadow pixels are also filtered out by a repeated minority
557 analysis in a 3-by-3 neighborhood, and then all shadows are buffered, with a width of 1 pixel, to
558 obtain the final shadow mask. The final shadow mask is combined with the final cloud mask to
559 get the final product of cloud and shadow mask.

560 561 3.6. Evaluation and comparison

562 To demonstrate the accuracy and effectiveness of the proposed method, it was compared with
563 Fmask (Zhu and Woodcock, 2012), one of the most advanced single-image methods and used by
564 USGS to produce the standard cloud mask for Landsat images. The results of Fmask can be
565 considered as a benchmark to assess the performance of ATSA. Both ATSA and Fmask were

566 applied to Landsat-8 OLI and Sentinel-2 images, while only ATSA was applied to Landsat-4 MSS
567 images in the second site, because MSS images lack not only thermal bands but also other bands
568 that are needed by Fmask. We found that Fmask detected many clouds as snow in some images in
569 the Hong Kong and Puerto Rico sites (Fig. 13). Because these two test sites are subtropical and
570 never have snow, we merged snow into clouds before the comparison, but this adjustment was not
571 made for cloud masks in Beijing site because it can snow in winter.

572



573

574 Fig. 13. Landsat-8 image DOY178 in the Puerto Rico site (a) and its original Fmask cloud mask
575 (b) showing where clouds are classified as snow (light blue color).

576

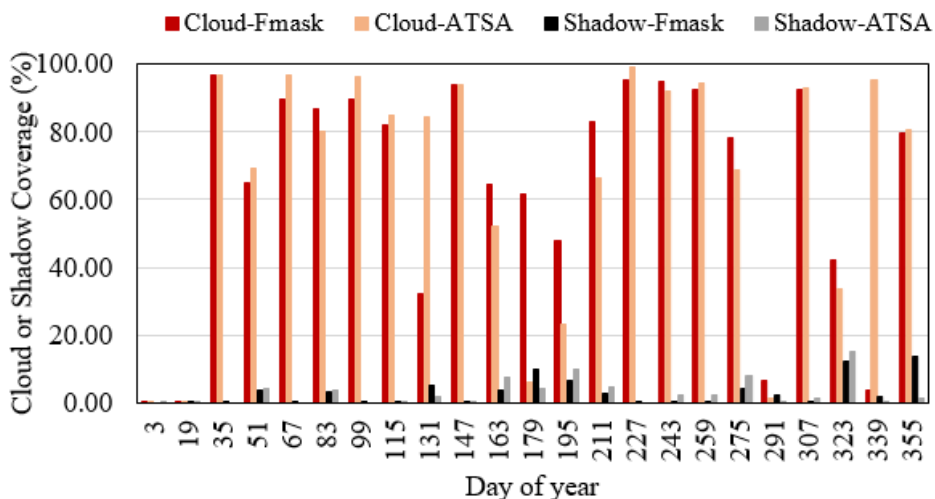
577 In the comparison, the agreement between these two methods was evaluated. First, the
578 percentage of clouds and cloud shadows of all methods were plotted together to check their
579 difference. Second, matrices were built comparing the proposed ATSA and Fmask methods, and
580 the overall agreement derived from these matrices was used to assess the pixel-wise agreement
581 between ATSA and Fmask. Third, representative images selected from the time series were
582 digitized to produce reference cloud and shadow masks. The digitizing work was done by
583 experienced experts who were not involved in the development of ATSA. Then, these digitized
584 maps were used to quantitatively evaluate the accuracy of both methods. It should be noted that

585 the manual mask of cloud and cloud shadow is not 100% accurate. It may include some
 586 commission or omission errors.

587 4. Results

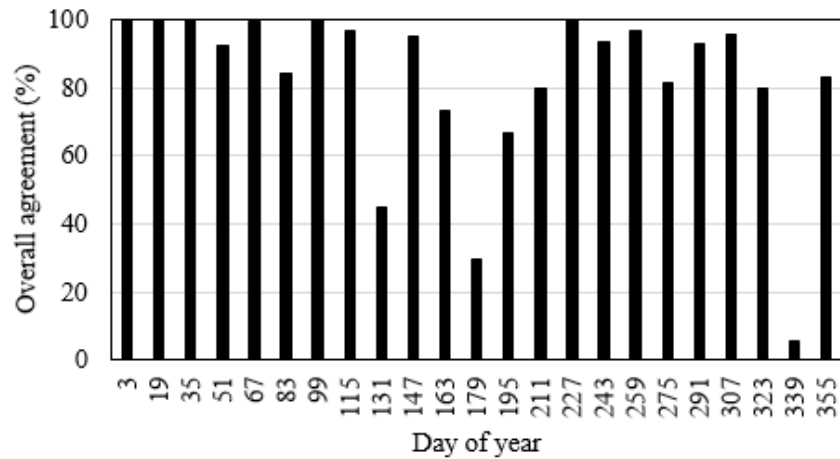
588 4.1. Hong Kong site

589 Among 23 images to which we applied the two cloud and shadow masking methods, the two
 590 methods detect similar cloud cover for 19 of them (Fig. 14), while for the other 4 images (DOY
 591 131, 179, 195, and 339) there are large differences. For the 19 images with similar cloud coverage,
 592 visual inspection confirms that both methods successfully detect clouds (see image of DOY 51 as
 593 an example in Fig. 16). For images of DOY 131 and 339, ATSA detected many more clouds than
 594 Fmask. On the other hand, for images of DOY 179 and 195, ATSA detected far fewer clouds than
 595 Fmask. Unlike cloud coverage, shadow coverage detected by the two methods slightly differs in
 596 most of the 23 images except the image DOY 355 (Fig. 14). Visual inspection of this image
 597 confirms that Fmask detected all water surface as cloud shadow. There are 5 images in the time
 598 series with large disagreement between ATSA and Fmask (Fig. 15). Agreement between ATSA and
 599 Fmask for the images of DOY 131, 179 and 339 is even lower than 50%.
 600



601

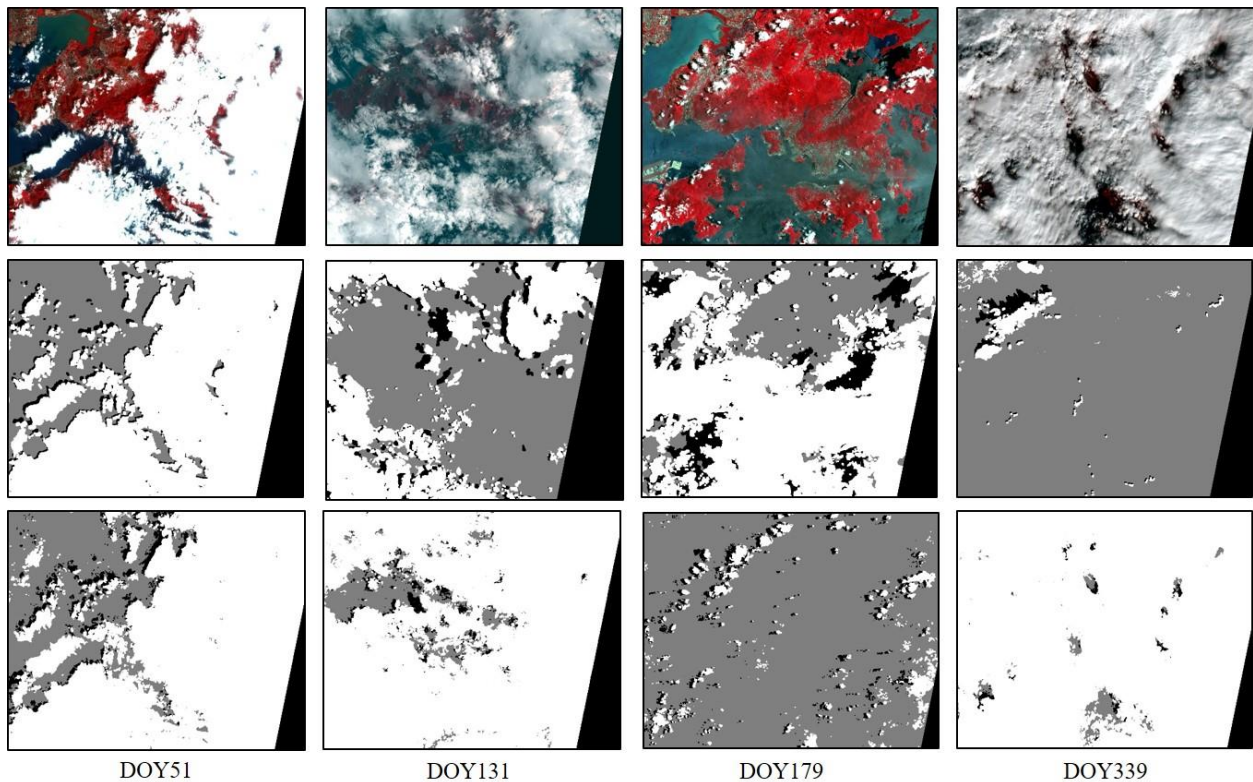
602 Fig. 14. Cloud and shadow coverage of 23 Landsat-8 OLI images in the Hong Kong site detected
 603 by ATSA and Fmask.



604
 605 Fig. 15. Overall agreement of cloud and shadow masks of 23 Landsat-8 OLI images in the Hong
 606 Kong site between ATSA and Fmask.

607
 608 In the cloud masks of the three images with the least agreement between ATSA and Fmask,
 609 it is clear from Fig. 16 that ATSA more accurately identified clouds. Fmask underestimated clouds
 610 in two images of DOY 131 and 339, and it overestimated clouds in the image of DOY 179.
 611 Specifically, Fmask failed to screen many of the thin clouds in the center of the image of DOY
 612 131, and it failed to identify many of the thick clouds in the image of DOY339, even though these
 613 clouds appear very bright in all visible and NIR bands. In the image of DOY179, Fmask
 614 misidentified most of the clear water and some clear land surface (see the island in the lower right)
 615 as clouds, which led to serious overestimation of cloud cover. For the cloud shadows, it appears
 616 that ATSA successfully identified most shadows adjacent to clouds. Fmask identified some clear
 617 pixels as shadow that were near the misidentified cloud patches (see image of DOY 179 in Fig.
 618 16).

619



620
 621 Fig. 16. False color composite of selected Landsat images (upper row) and their cloud masks by
 622 Fmask (middle row) and ATSA (lower row) for the Hong Kong site (gray: clear pixels; black:
 623 shadows; white: clouds)

624
 625 Quantitative accuracy assessment for the four images in Fig. 16 using manual masks shows
 626 that ATSA and Fmask obtain comparable overall accuracy for the image of DOY51, but ATSA's
 627 overall accuracy is much higher than Fmask for the other three images (Table 4). For cloud
 628 detection, ATSA obtained user's accuracies ranging from 0.85 to 0.99 and producer's accuracies
 629 ranging from 0.89 to 0.99. The accuracy of ATSA cloud mask for the image of DOY179 is lower
 630 than that of the other images due to the errors in haze detection on the water surface (see haze in
 631 the lower right part of this image). In contrast, the cloud producer's accuracy of Fmask is low for
 632 images of DOY131 (0.41) and DOY339 (0.04) because of large omission errors. The cloud user's

633 accuracy of Fmask is low for images of DOY179 (0.08) because it misidentified many clear pixels
 634 as clouds. For shadow detection, ATSA can obtain producer’s accuracy higher than 0.82. The
 635 shadow user’s accuracy is also high except the image of DOY179, in which ATSA overestimated
 636 the shadow area. In the context of applications with cloudy images, the producer’s accuracy is
 637 more important than user’s accuracy, because end users hope to exclude all contaminated pixels in
 638 their analysis, and meanwhile they can allow commission errors to some extent (Zhu and
 639 Woodcock, 2012). Both user’s and producer’s accuracies of shadow detection by Fmask are much
 640 lower than ATSA. Specifically, Fmask detected fewer shadows in the image of DOY51 and
 641 identified clear pixels near the wrong cloud patches as shadow in other three images in Fig. 16.

642
 643
 644
 645
 646

647 Table 4 Accuracy assessment of cloud masks of the 4 images in Fig. 16 in the Hong Kong site:
 648 overall accuracy (*oa*), user’s accuracy (*ua*) and producer’s accuracy (*pa*).

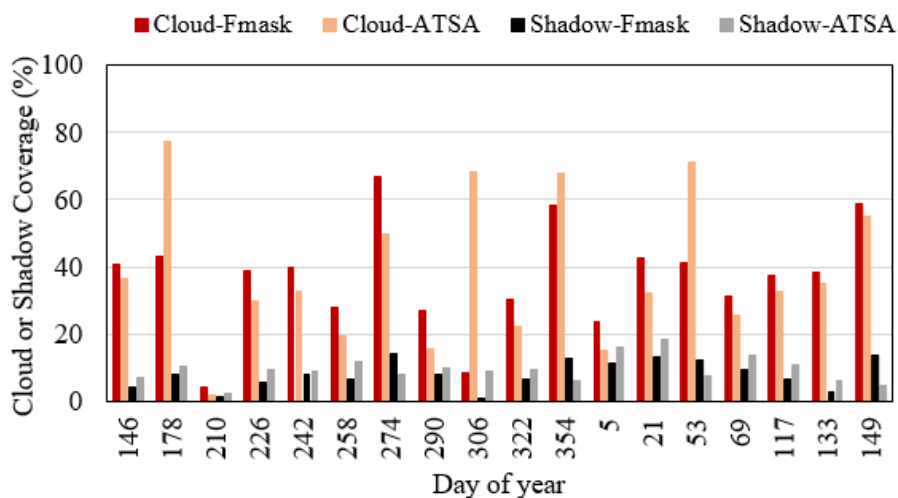
DOY		Cloud			Shadow	
		<i>oa</i>	<i>Ua</i>	<i>pa</i>	<i>ua</i>	<i>pa</i>
51	Fmask	0.93	0.97	0.98	0.60	0.49
	ATSA	0.99	0.99	0.99	0.95	0.87
131	Fmask	0.45	0.99	0.41	0.04	0.10
	ATSA	0.98	0.99	0.99	0.93	0.82
179	Fmask	0.29	0.08	0.98	0.08	0.26
	ATSA	0.97	0.85	0.89	0.67	0.90
339	Fmask	0.06	0.95	0.04	0.00	0.00
	ATSA	0.99	0.99	1.00	0.89	1.00

649

650 4.2. Puerto Rico site

651 4.2.1. Landsat-8 OLI images

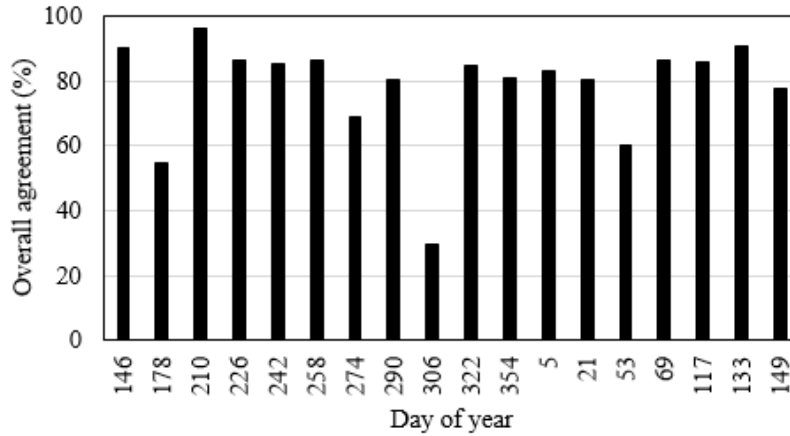
652 Among the 18 images, ATSA and Fmask obtained similar cloud coverage in 15 images, while
 653 ATSA detected many more clouds in three images (DOY178(2013), 306(2013), and 053(2014))
 654 than Fmask (Fig. 17). For shadow coverage, ATSA detected slightly more shadows than Fmask in
 655 most images. Through visual inspection of these images, we found that Fmask underestimated
 656 shadows surrounding small cloud patches, which leads to smaller shadow percentage than ATSA.
 657 On the other hand, in the images DOY 274(2013), 354(2013), 53(2014), and 149(2014), ATSA
 658 detected fewer shadows than Fmask. Visual inspection shows that these four images only have
 659 large cloud patches. Fmask overestimated shadow cover of these large cloud patches. The
 660 quantitative assessment of pixel-wise agreement between the two methods is good (higher than
 661 80%) for masks of most images, but the masks of two images, DOY 178(2013) and 306(2013)
 662 have agreement between ATSA and Fmask that is lower than 60% (Fig. 18). For the images with
 663 good agreement between ATSA and Fmask, both methods successfully detect clouds (e.g. image
 664 DOY146(2013) in Fig. 19). In the two images with the least agreement between ATSA and Fmask,
 665 Fmask omitted a lot of thin clouds in west region in the image of DOY178(2013), and it missed a
 666 lot of cloudy pixels, even of thick clouds, in the image of DOY306(2013) (Fig. 19).



667

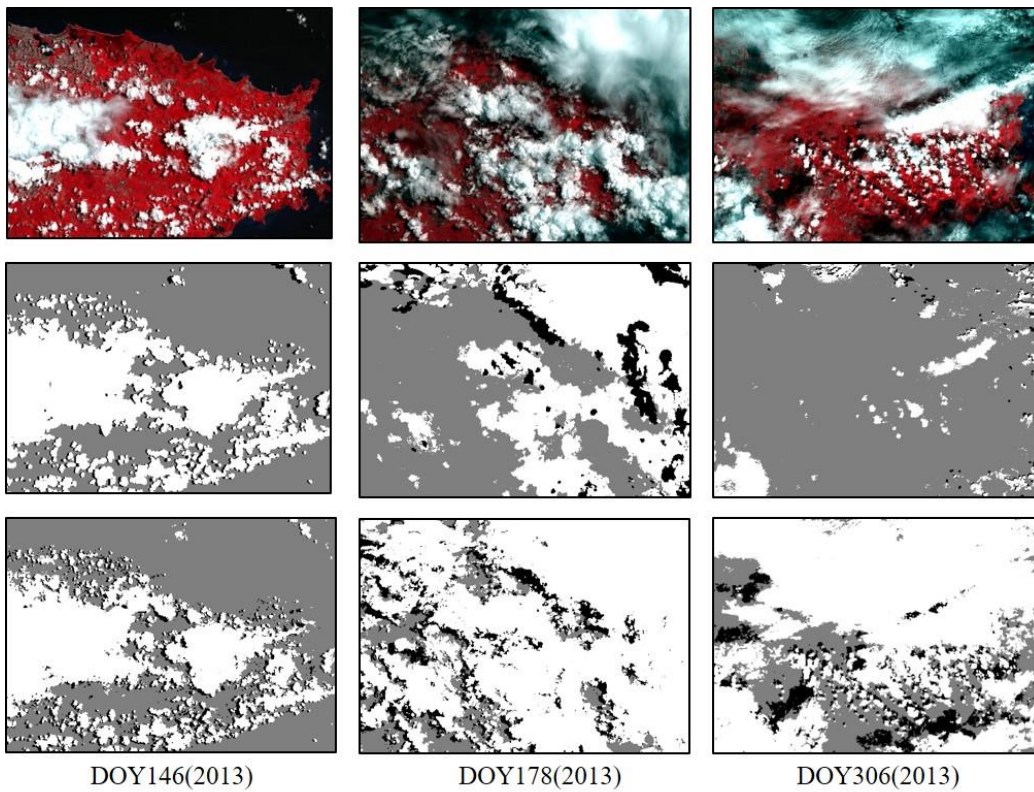
668 Fig. 17. Cloud and shadow coverage of 18 Landsat-8 OLI images in the Puerto Rico site detected
 669 by ATSA and Fmask

670



671

672 Fig. 18. Overall agreement of cloud and shadow mask between ATSA and Fmask for the Puerto
 673 Rico site.



674

675 Fig. 19. False color composite of the three Landsat images in the Puerto Rico site (upper row)

676 and their cloud and shadow masks by Fmask (middle row) and ATSA (lower row) (gray: clear
 677 pixels; black: shadows; white: clouds)

678 The quantitative accuracy assessment of the cloud masks of these three images in Fig. 19,
 679 using manual masks, shows that the overall accuracy of ATSA cloud and shadow masks ranges
 680 from 0.97 to 0.98, which is much higher than Fmask (Table 5). Cloud producer’s and user’s
 681 accuracy of ATSA reaches 0.97 in all three images, while cloud producer’s accuracies of Fmask
 682 are only 0.12 to 0.52 for the image of DOY178 and 306. Shadow producer’s and user’s accuracies
 683 of ATSA are lower than the cloud mask accuracy, but it is still much higher than Fmask. ATSA
 684 omitted some thin shadows on land surfaces in the lower part of image of DOY306 (Fig. 19)
 685 leading to a relatively lower producer’s accuracy of 0.86. Similar to the Hong Kong site, Fmask
 686 detected fewer shadows than the real situation, leading to low producer’s accuracy in shadow
 687 detection.

688
 689 Table 5. Accuracy assessment of cloud masks of three images in Fig. 19 in the Puerto Rico site:
 690 overall accuracy (*oa*), user’s accuracy (*ua*) and producer’s accuracy (*pa*).

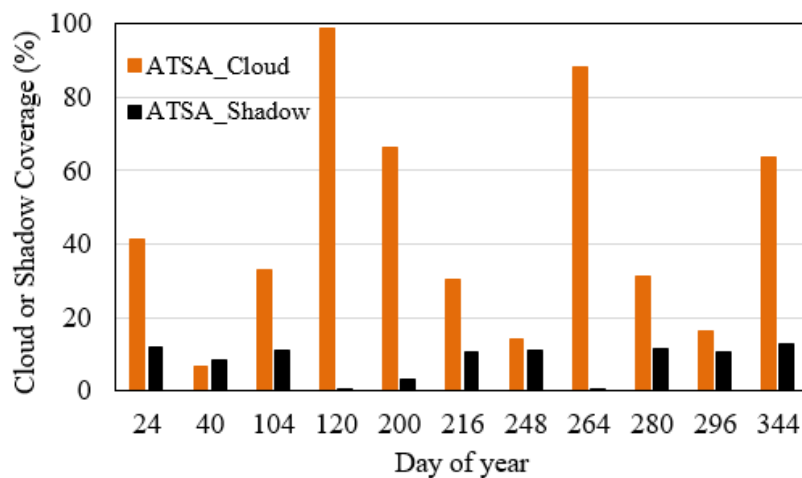
DOY(Year)		Cloud			Shadow	
		<i>oa</i>	<i>ua</i>	<i>pa</i>	<i>ua</i>	<i>pa</i>
146(2013)	Fmask	0.90	0.85	0.98	0.58	0.34
	ATSA	0.98	0.97	1.00	0.92	0.94
178(2013)	Fmask	0.53	0.98	0.52	0.07	0.08
	ATSA	0.98	0.98	0.99	0.97	0.96
306(2013)	Fmask	0.28	0.98	0.12	0.03	0.00
	ATSA	0.97	1.00	0.98	0.97	0.86

691

692 4.2.2. Landsat-4 MSS images

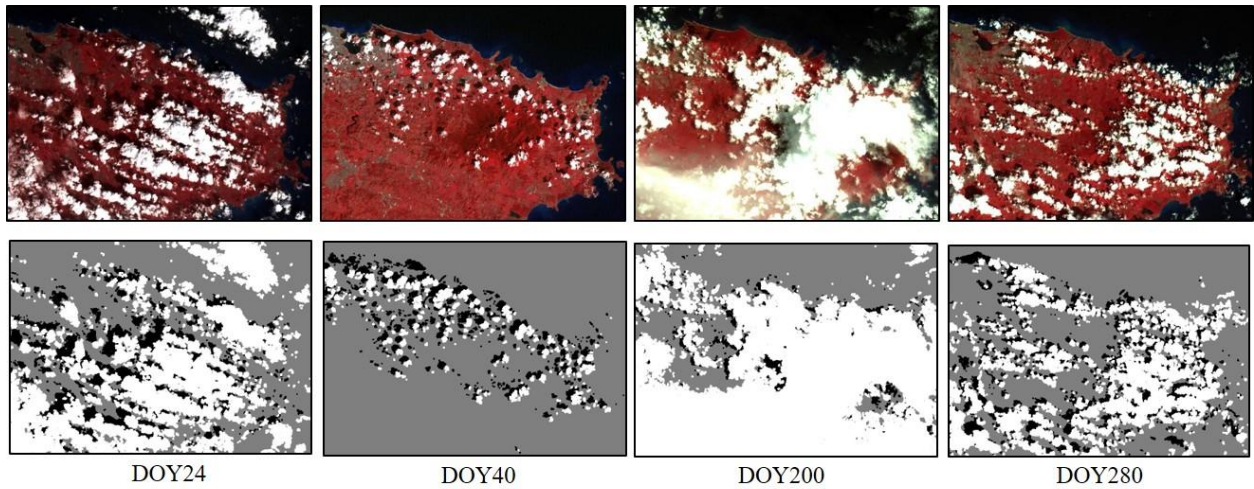
693 Only ATSA was applied to the 11 Landsat-4 MSS images in the Puerto Rico site, because
 694 Fmask needs more bands than MSS images have. Four images with representative cloud coverages

695 (6.8% to 99% clouds; 0% to 12.6% cloud shadows) were selected for further assessment (Fig. 20).
 696 The cloud coverages of these four selected images are 6.8% (DOY40), 31.1% (DOY280), 41.4%
 697 (DOY24), and 66.1% (DOY200). Visual inspection shows that ATSA successfully identified most
 698 clouds and shadows in these MSS images (Fig. 21), including the thin clouds in the image of
 699 DOY200. We can see that the cloud user's and producer's accuracy of all four MSS images are
 700 higher than 0.95 (Table 6), indicating that ATSA successfully screened clouds in these images with
 701 very small omission and commission errors. For shadow accuracy, in terms of producer's accuracy
 702 (more important for applications in our opinion), it is high enough in image DOY 40, and 280,
 703 reaching 0.97. The image DOY200 has shadow producer's accuracy of 0.83 which is caused by
 704 the identification of shadows as clouds in the lower right part of this image (Fig. 21).



705
 706 Fig. 20. Cloud and shadow coverage of 11 Landsat MSS images in the Puerto Rico site detected
 707 by ATSA.

708



709

710 Fig. 21. False color composite of the four representative Landsat MSS images in the Puerto Rico
 711 site and their cloud and shadow masks by ATSA (gray: clear pixels; black: shadows; white:
 712 clouds).

713

714

715

716 Table 6. Accuracy assessment of cloud masks of four MSS images in Fig. 21 in the Puerto Rico
 717 site: overall accuracy (*oa*), user's accuracy (*ua*) and producer's accuracy (*pa*)

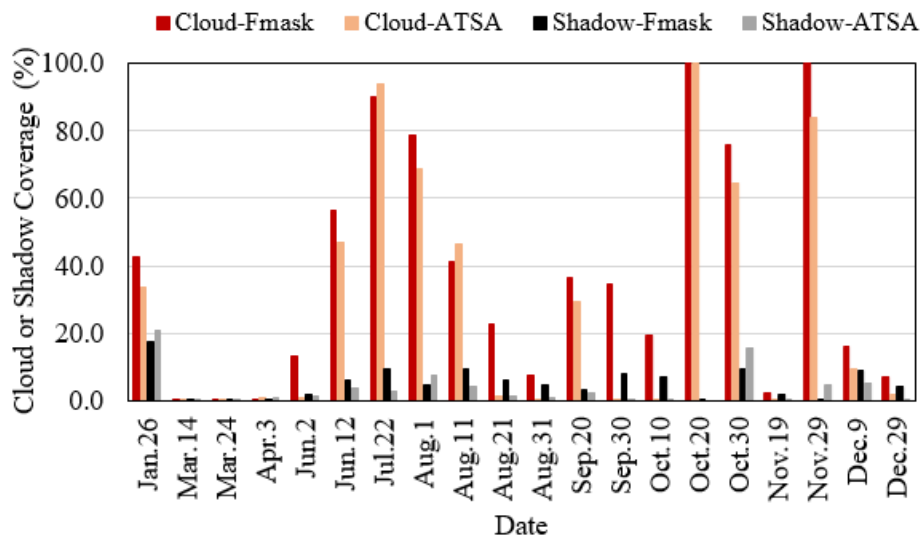
DOY	Cloud			Shadow	
	<i>oa</i>	<i>Ua</i>	<i>pa</i>	<i>ua</i>	<i>pa</i>
24	0.96	0.98	0.99	0.88	0.87
40	0.99	1.00	0.99	0.89	1.00
200	0.97	0.99	0.97	0.90	0.83
280	0.98	1.00	0.98	0.92	0.97

718

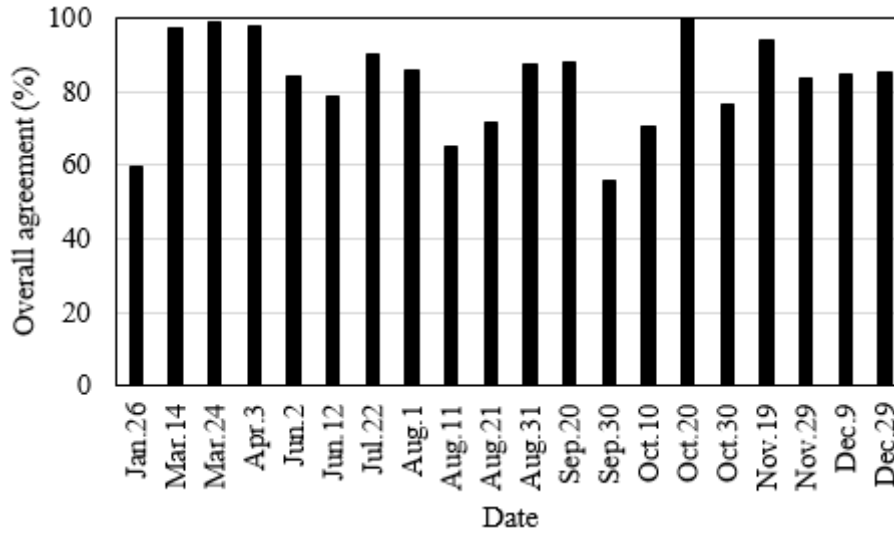
719 4.3. Beijing site

720 In general, the cloud coverage detected by ATSA is smaller than that of Fmask in the 20
 721 Sentinel-2 images. The cloud coverage difference between ATSA and Fmask is larger than or equal
 722 to 20% in three images, Aug. 21, Sep.30, and Oct.10 (Fig. 22). Through visual inspection of these

723 cloud masks, we found that both ATSA and Fmask misclassify some pixels in very bright urban
 724 surfaces as clouds, but this commission error of Fmask is more serious than ATSA. Fmask detected
 725 nearly all urban pixels as cloud or snow in the three images of Aug.21, Sep.30, and Oct.10. Similar
 726 to cloud coverage, shadow coverage detected by ATSA is generally lower than Fmask, except for
 727 images dated Oct. 30 and Nov. 29. The larger shadow coverage detected by Fmask results from
 728 the commission errors of cloud detection. In other words, Fmask detected many clear pixels as
 729 shadow surrounding areas wrongly detected as clouds. Regarding the pixel-wise agreement
 730 between ATSA and Fmask (Fig. 23), there are 7 images with overall agreement lower than 80%
 731 and 3 images lower than 70%. These three images are Jan.26, Aug.11, and Sep.30.



732
 733 Fig. 22. Cloud and cloud shadow coverage of 20 Sentinel-2 images in the Beijing site detected
 734 by ATSA and Fmask.



735

736 Fig. 23. Overall agreement of cloud and shadow mask between ATSA and Fmask for the 20

737 Sentinel-2 images from the Beijing site.

738

739 For the images with high agreement between ATSA and Fmask, both methods successfully

740 detect clouds and shadows (see Sep.20 image as an example in Fig. 24). In the three images with

741 the least agreement between ATSA and Fmask, ATSA is generally more successful than Fmask for

742 identifying clouds and shadows. Specifically, in the Jan. 26 image, both ATSA and Fmask detected

743 most of clouds. ATSA does not have snow detection step, so the snow in the northwest was

744 misclassified as cloud in ATSA, while Fmask successfully detected these snows but it also

745 identified many clear pixels as snow. Fmask also detected many clear and thin-cloudy pixels as

746 snow in summer image where no snow events should happen. In addition, Fmask detected many

747 clear urban pixels as cloud in the Sep. 30 image (Fig. 24). For cloud shadow detection, ATSA is

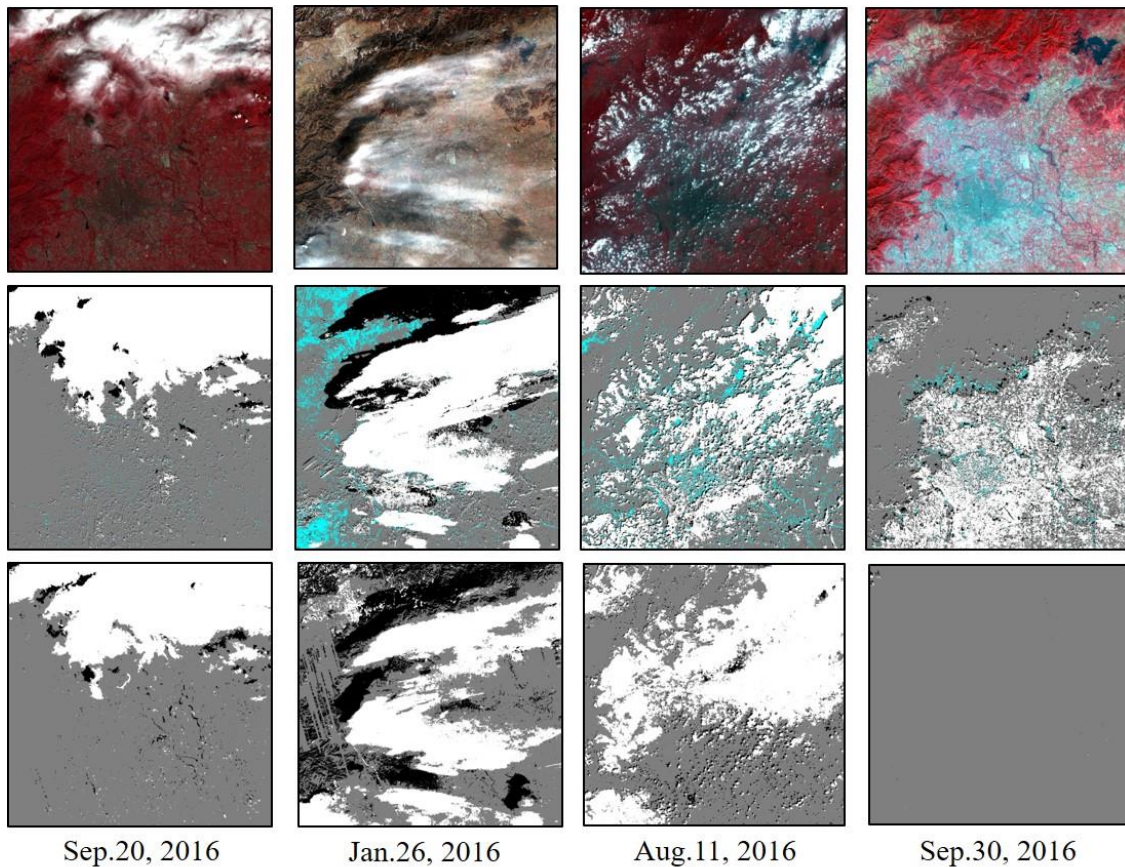
748 more successful although it detected topographic shadows as cloud shadows in the Jan. 26 image.

749 Images of mountainous areas have more topographic shadows in spring and winter due to the lower

750 sun elevation. It may lead to larger commission errors in cloud shadow detection if these

751 topographic shadows are within the potential shadow zones. In contrast, Fmask failed to detect

752 shadows which are distant from the cloud patches. The possible reason is that Fmask for Sentinel-
753 2 assumes the cloud height between 200 m and 1,200 m for all images (Zhu et al., 2015).



754
755 Fig. 24. False color composite of the four Sentinel-2 images in the Beijing site (upper row) and
756 their cloud mask by Fmask (middle row) and ATSA (lower row) (gray: clear pixels; black:
757 shadows; white: clouds; snow: light blue)

758
759 The quantitative accuracy assessment also demonstrates that ATSA can obtain more accurate
760 cloud and shadow masks than Fmask (Table 7). For the Sep. 20 image, both ATSA and Fmask can
761 obtain acceptable accuracy in cloud detection. For other three images, cloud producer's accuracy
762 of ATSA ranges from 0.81 to 0.96 and cloud user's accuracy ranges from 0.92 to 0.99. In contrast,
763 cloud user's accuracy of Fmask for the Sep.30 image is very low because of large commission

764 errors, and the low cloud producer's accuracy of Fmask for the Aug.11 image is caused by large
 765 omission errors. For the Jan. 26 image, the producer's accuracy of cloud detection for both Fmask
 766 and ATSA is only 0.81 because both methods omitted extremely thin clouds. For shadow detection,
 767 ATSA obtains good producer's accuracy ranging from 0.81 to 0.96, which is much higher than
 768 Fmask ranging from 0.20 to 0.50, indicating that Fmask omitted considerable cloud shadow in
 769 these images. For the Jan. 26 image, the user's accuracy of shadow detection by ATSA is only 0.5,
 770 because it detects many black rocks and topographic shadows as cloud shadows. In this
 771 mountainous area, some snow and ice pixels were misclassified as clouds, which makes the black
 772 rocks and topographic shadows within the potential shadow zone. This issue can be solved if the
 773 commission error in cloud detection is reduced, especially for distinguishing snow and ice from
 774 clouds.

775

776 Table 7. Accuracy assessment of cloud masks of images in Fig. 24: overall accuracy (*oa*), user's
 777 accuracy (*ua*) and producer's accuracy (*pa*).

Date		Cloud			Shadow	
		<i>oa</i>	<i>ua</i>	<i>pa</i>	<i>ua</i>	<i>pa</i>
Sep.20	Fmask	0.89	0.80	1.00	0.20	0.41
	ATSA	0.98	0.99	1.00	0.62	0.81
Jan.26	Fmask	0.67	0.74	0.81	0.33	0.50
	ATSA	0.79	0.92	0.81	0.50	0.87
Aug.11	Fmask	0.68	0.77	0.65	0.21	0.46
	ATSA	0.97	0.99	0.96	0.94	0.86
Sep.30	Fmask	0.58	0.00	0.92	0.00	0.20
	ATSA	1.00	0.99	0.85	0.96	0.96

778

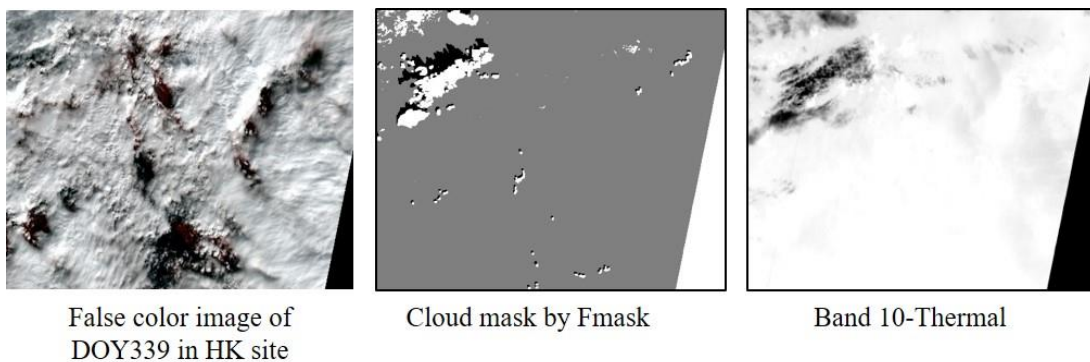
779 5. Discussion and conclusions

780 Masking clouds and cloud shadows is necessary for many applications of optical satellite
 781 images, because it is difficult to acquire totally cloud-free images in most places, particularly when

782 time series are needed to monitor change. Many methods have been developed to screen clouds
783 and cloud shadows automatically in optical images. However, they may not perform well in very
784 cloudy regions. Aiming to produce more accurate cloud and shadow masks of optical imagery in
785 cloudy regions, an automatic time series analysis based method, ATSA, was developed in this study.
786 ATSA was tested in three sites with different dominant land covers. Landsat-8 OLI images,
787 Landsat-4 MSS images, and Sentinel-2 images were used to evaluate the performance of ATSA
788 for screening clouds and cloud shadows in images with different band configurations and quality.
789 Results show that ATSA can obtain accurate cloud and shadow masks in all sites and all data sets
790 except the images with snow and ice cover. The comparison with an advanced algorithm, Fmask,
791 also confirms that ATSA can yield robust and accurate cloud and shadow masks in cloudy regions.
792 The good performance of ATSA can be attributed to the following strengths.

793 First, ATSA only needs a minimum number of input bands. Only 5 bands, blue, green, red,
794 NIR, and SWIR bands, are required, and this requirement can be reduced to 3 bands if the images
795 do not have blue and SWIR bands. The low requirement of input bands brings two advantages.
796 The first advantage is that in the regions tested, the results can be more robust than existing
797 methods when processing images with various conditions. Although the spectral similarities
798 among different land surfaces and clouds and cloud shadows are complex, being different among
799 locations and times, a common characteristic is that they affect the pixel values from visual to near
800 infrared bands, i.e., clouds brighten these bands and shadows darken them. In general, adding more
801 bands into the screening process, such as thermal bands or a cirrus band, can improve the accuracy
802 of cloud and shadow masks, especially for the single-image cloud detection methods (Foga et al.,
803 2017; Zhu et al., 2015). However, it may also lead to more uncertainties and errors in some extreme
804 cases. For example, Fmask uses visible, near infrared, and thermal bands to identify clouds; it also

805 uses the cirrus band in Landsat-8 images to detect clouds (Zhu et al., 2015), while ATSA uses
806 neither the thermal nor cirrus bands. In the Hong Kong site, for the image DOY339, Fmask misses
807 most clouds. A further investigation of all bands of this image reveals that the thermal band is
808 cooler in a small sub-area of this mostly cloudy image (Fig. 25). As a result, Fmask only detects
809 clouds in this cold area and omits other warmer clouds. According to the USGS product guide,
810 Fmask has a known issue that either too large or too small temperature differentials will lead to
811 errors in cloud detection. The second advantage of using fewer bands is that the algorithm is more
812 flexible and applicable than existing methods when processing images from different optical
813 sensors. For cloudy places, we expect ATSA to: (1) extend the history for automated Landsat time
814 series analyses with cloud and cloud shadow masks that are highly accurate, but automatically
815 derived, back to the MSS era of the 1970s (instead of only the TM era of the 1980s); and (2) in the
816 era of Sentinel-2, allow for denser time series in intra-annual analyses such as those examining
817 vegetation phenology. The past and ongoing optical sensors have different configurations of
818 spectral bands. However, most of these optical sensors have visible and near infrared bands. ATSA
819 can be applied to all images with these basic bands, which is very important and necessary when
820 we process historical satellite images with limited bands.

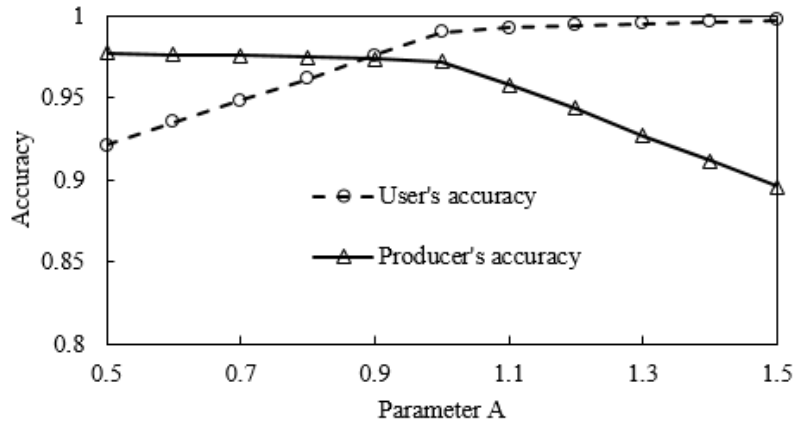


822 Fig. 25. False color composite of the Landsat-8 images DOY339 in the Hong Kong site (left), its
823 cloud mask by Fmask (center), and the thermal band of this image (right)

824

825 Second, ATSA has fewer predefined parameters than most existing methods. In ATSA, there
826 are only two important predefined parameters, i.e., A in Eq. (8) and B in Eq. (12) tune the threshold
827 for identifying clouds and shadows in the time series respectively. As standard deviation
828 multipliers of variation through the time series, these two parameters regulate the degree of
829 strictness for masking clouds and shadows. In other words, they balance the omission errors and
830 commission errors of cloud and shadow detection. In our tests, A and B are 0.5 and 1.5 for the
831 Hong Kong site, 1.0 and 1.5 for the Puerto Rico site, and 1.2 and 2.0 for the Beijing site. Fig. 26
832 shows the cloud user's and producer's accuracy for the Landsat-4 MSS image DOY200 in Fig. 21
833 when using different values of parameter A within the recommended range 0.5-1.5. Larger values
834 of parameter A improve the user's accuracy but meanwhile decrease the producer's accuracy. The
835 parameter B shows a similar effect on the accuracy of cloud shadow detection. Fig. 26 also suggests
836 that the detection accuracy is not very sensitive to the parameter. There is a wide range of parameter
837 A able to obtain both producer's accuracy and user's accuracy higher than 0.95. Users can tune
838 these two parameters according to their specific applications. For example, studies using time
839 series to model land surface parameters, such as forest biomass and crop yield, are very sensitive
840 to clouds, even the extremely thin clouds. These studies may hope to mask out all possible clouds
841 and accept some commission errors, so smaller values of parameter A and B should be used. In
842 addition, ATSA also use the statistics of each image in the time series to determine some parameters
843 to increase the adaptability of ATSA. For example, the HOT transformation has been used in many
844 cloud screening methods, such as MFC (Li et al., 2017) and Fmask (Zhu and Woodcock, 2012).
845 However, these methods apply one HOT formula to all images. For instance, both MFC and Fmask
846 use $HOT=B_{blue}-0.5B_{red}$ for all images. However, the coefficients in the HOT transformation vary

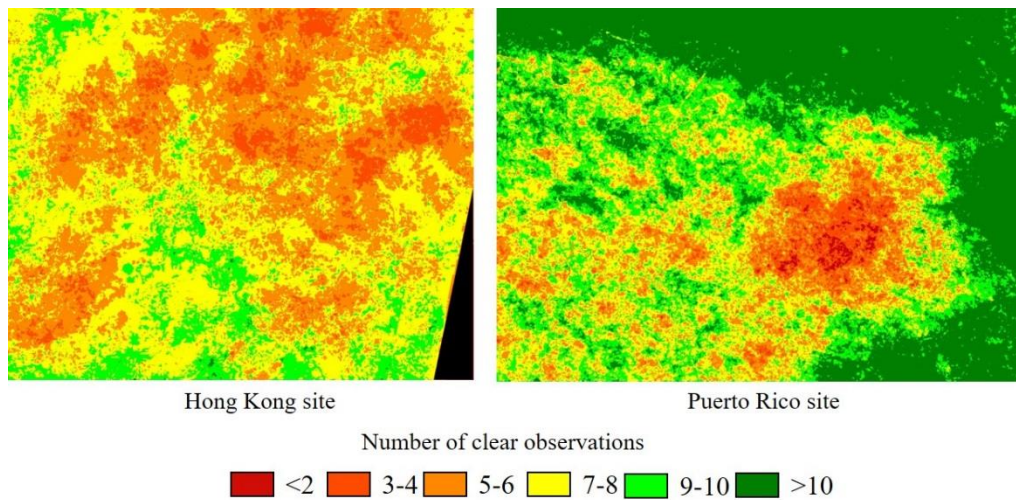
847 from scene-to-scene, so it is necessary to estimate the HOT parameter for individual images (Chen
848 et al., 2016; Zhang et al., 2002). ATSA regresses the coefficients in HOT transformation model in
849 each image by an automated strategy which can get optimal cloud index images.



850
851 Fig. 26. User's and producer's accuracy of cloud detection for the Landsat-4 MSS image
852 DOY200 in the Puerto Rico site using different values of parameter A

853
854 Third, ATSA uses the minimal clear observations in image time series over cloudy regions to
855 ensure accurate cloud and shadow masking without fitting a time series model of these
856 observations. For both cloud and shadow detection, there are two hierarchies in ATSA. In the first
857 hierarchy, ATSA selects samples from all images in the time series for optimizing the class centers
858 in the K-means classifier. As we know, it is quite common that image scenes are totally covered
859 by clouds. If the K-means classifier ($K=2$ or 3) is applied to each individual image, it cannot detect
860 all clouds in a totally cloud-covered image. In the second hierarchy, ATSA only uses "clear"
861 observations in the time series to estimate the adaptive threshold, and further detect clouds and
862 shadows omitted in the first hierarchy. Another multi-temporal method, Tmask, also uses clear
863 observations in the time series to refine the initial cloud mask from Fmask. It can detect more thin
864 clouds than Fmask (Zhu and Woodcock, 2014). However, Tmask is not appropriate in our test sites

865 in cloudy regions. Fig. 27 shows the number of clear observations of individual pixels in the time-
 866 series data of Hong Kong and Puerto Rico site. We can see that both sites have considerable pixels
 867 with fewer than 6 clear observations. The clear observations are not enough for Tmask (15 clear
 868 observations are recommended) to accurately estimate the parameters in the time series model,
 869 leading to misclassifying cloudy pixels as clear pixels (Foga et al., 2017). Unlike Tmask, ATSA
 870 does not fit a time series model using many clear observations. It can be an alternative to Tmask
 871 for screening clouds in time-series data of cloudy regions or short time series (e.g., one year) which
 872 is unlikely to have enough clear observations.



873 Fig. 27. Number of clear observations of individual pixel in the Landsat-8 time series at both
 874 Hong Kong and Puerto Rico sites.
 875

876
 877 There are also some limitations in ATSA. First, ATSA currently does not have a snow
 878 detection module. In tropical and subtropical regions, which are among the cloudiest regions (Ju
 879 and Roy, 2008), images in these regions do not have snow in all seasons except at the highest
 880 elevations. If the images include snow, ATSA is likely to detect snow as clouds (see Jan.26 image
 881 in Fig. 24). This outcome may be acceptable in many applications, such as vegetation studies, in
 882 which, like clouds, snow would often be excluded. Actually, most current algorithms often confuse

883 snow and clouds even if they have a snow detection module, like the Fmask results shown in Fig.
884 13 and Fig. 24. If more powerful snow detection methods are developed in the future, they can be
885 integrated with ATSA. Second, although the HOT transformation can suppress the pixel values of
886 various land covers (also see an experiment in a desert landscape shown in the Supplementary
887 Data), the very bright pixels may be identified as clouds. A recent study proposed an iterative HOT
888 (IHOT) algorithm which can better suppress surface reflectance (Chen et al., 2016), but it needs
889 more computing time. IHOT can be used as an alternative to HOT if the computing time is not a
890 restriction factor. Third, land cover changes may happen in the time series. It may bring temporal
891 variability in the HOT time series which could further affect the cloud detection by ATSA. An
892 experiment reported in the Supplementary Data shows that ATSA may be not affected by many
893 types of land cover changes, but other methods (e.g. Tmask) which can model land cover change
894 may obtain better results than ATSA when substantial land cover changes exist. Fourth, ATSA may
895 omit some cloud shadows on water surfaces or cloud shadows on the land surface that are
896 extremely thin. Omission of cloud shadows on water surfaces may not affect mapping the water
897 bodies, but it may affect water quality modeling. Thin cloud shadow on land surfaces may also
898 affect quantitative information retrieval. Omission errors from missed cloudy pixels are the most
899 common errors in cloud shadow masking methods (Foga et al., 2017); however, more accurate
900 cloud detection with ATSA in the types of landscapes tested should reduce this error. These errors
901 can be corrected by a further manual checking. Fifth, ATSA requires a time series, albeit with fewer
902 dates than existing methods. Last, due to the limitation of resources and support, ATSA was tested
903 in several typical sites and on data sets from three satellite sensors. More comparison and
904 validation are needed, and they are our future studies. Due to its simple principles, ATSA has an
905 acceptable efficiency for processing time-series data. ATSA only used 11 minutes and 13 minutes

906 for the Landsat-8 time series in Hong Kong and Puerto Rico sites respectively (program coded in
907 interactive data language and run on a windows laptop with a 2.50GHz CPU and 8 GB RAM). We
908 welcome other researchers to test ATSA in more areas and different data sets. The code of ATSA
909 is available upon request.

910 In conclusion, a new cloud and cloud shadow screening method, ATSA, was developed in
911 this study. Its target is time series optical images in cloudy regions. ATSA is a valuable supplement
912 to the family of cloud and cloud shadow masking algorithms. It will support studies of land surface
913 dynamics using dense optical time series, such as studies of forest phenology in tropical regions
914 using Landsat or Sentinel-2 images.

915

916 **Acknowledgements**

917 This study was supported by the Research Grants Council of Hong Kong (project no.25222717),
918 the National Natural Science Foundation of China (project no.41701378), the grant 1-ZE6Q from
919 The Hong Kong Polytechnic University, the USDA Forest Service International Institute of
920 Tropical Forestry (Cooperative Agreement 13-CA-11120101-029), the Southern Research Station
921 Forest Inventory and Analysis Program, and the National Science Foundation of the USA
922 (1010314). We thank Dr. Zhe Zhu at Texas Tech University for sharing the Fmask code and for his
923 assistance during the implementation of Fmask. We thank Yujing Chen, Jiaqi Tian, and Zheyang
924 Shen for creating cloud reference data. We also thank Ronn Kling for his earlier input on cloud
925 and cloud shadow masking.

926

927 **Appendix A. Supplementary data**

928 Supplementary data to this article can be found online at ##.

930 **References**

- 931 Bassett, G.J., Koenker, R., 1978. Asymptotic Theory of Least Absolute Error Regression. *J. Am.*
932 *Stat. Assoc.* 73, 618–622. doi:10.2307/2286611
- 933 Cahalan, R., Oreopoulos, L., Wen, G., Marshak, A., Tsay, S.-C., DeFelice, T., 2001. Cloud
934 characterization and clear-sky correction from Landsat-7. *Remote Sens. Environ.* 78, 83–98.
935 doi:10.1016/S0034-4257(01)00251-6
- 936 Chen, J., Chen, J., Liao, A., Cao, X., Chen, L., Chen, X., He, C., Han, G., Peng, S., Lu, M., Zhang,
937 W., Tong, X., Mills, J., 2015. Global land cover mapping at 30m resolution: A POK-based
938 operational approach. *ISPRS J. Photogramm. Remote Sens.* 103, 7–27.
939 doi:10.1016/j.isprsjprs.2014.09.002
- 940 Chen, S., Chen, X., Chen, J., Jia, P., Cao, X., Liu, C., 2016. An Iterative Haze Optimized
941 Transformation for Automatic Cloud/Haze Detection of Landsat Imagery. *IEEE Trans.*
942 *Geosci. Remote Sens.* 54, 2682–2694. doi:10.1109/TGRS.2015.2504369
- 943 Choi, H., Bindschadler, R., 2004. Cloud detection in Landsat imagery of ice sheets using shadow
944 matching technique and automatic normalized difference snow index threshold value decision.
945 *Remote Sens. Environ.* 91, 237–242. doi:10.1016/j.rse.2004.03.007
- 946 Fisher, A., 2013. Cloud and cloud-shadow detection in SPOT5 HRG imagery with automated
947 morphological feature extraction. *Remote Sens.* 6, 776–800. doi:10.3390/rs6010776
- 948 Foga, S., Scaramuzza, P.L., Guo, S., Zhu, Z., Dilley, R.D., Beckmann, T., Schmidt, G.L., Dwyer,
949 J.L., Joseph Hughes, M., Laue, B., 2017. Cloud detection algorithm comparison and
950 validation for operational Landsat data products. *Remote Sens. Environ.* 194, 379–390.
951 doi:10.1016/j.rse.2017.03.026
- 952 Goodwin, N.R., Collett, L.J., Denham, R.J., Flood, N., Tindall, D., 2013. Cloud and cloud shadow
953 screening across Queensland, Australia: An automated method for Landsat TM/ETM+ time
954 series. *Remote Sens. Environ.* 134, 50–65. doi:10.1016/j.rse.2013.02.019
- 955 Hagolle, O., Huc, M., Pascual, D.V., Dedieu, G., 2010. A multi-temporal method for cloud
956 detection, applied to FORMOSAT-2, VEN μ S, LANDSAT and SENTINEL-2 images. *Remote*
957 *Sens. Environ.* 114, 1747–1755. doi:10.1016/j.rse.2010.03.002
- 958 Hansen, M.C., Loveland, T.R., 2012. A review of large area monitoring of land cover change using
959 Landsat data. *Remote Sens. Environ.* 122, 66–74. doi:10.1016/j.rse.2011.08.024
- 960 Helmer, E.H., Ruefenacht, B., 2007. A comparison of radiometric normalization methods when
961 filling cloud gaps in Landsat imagery. *Can. J. Remote Sens.* 33, 325–340. doi:10.5589/m07-
962 028
- 963 Helmer, E.H., Ruefenacht, B., 2005. Cloud-free satellite image mosaics with regression trees and
964 histogram matching. *Photogramm. Eng. Remote Sens.* 71, 1079–1089.
965 doi:10.14358/PERS.71.9.1079
- 966 Helmer, E.H., Ruzycski, T.S., Benner, J., Voggesser, S.M., Scobie, B.P., Park, C., Fanning, D.W.,

967 Ramnarine, S., 2012. Detailed maps of tropical forest types are within reach: Forest tree
968 communities for Trinidad and Tobago mapped with multiseason Landsat and multiseason
969 fine-resolution imagery. *For. Ecol. Manage.* 279, 147–166. doi:10.1016/j.foreco.2012.05.016

970 Huang, C., Thomas, N., Goward, S.N., Masek, J.G., Zhu, Z., Townshend, J.R.G., Vogelmann, J.E.,
971 2010. Automated masking of cloud and cloud shadow for forest change analysis using
972 Landsat images. *Int. J. Remote Sens.* 31, 5449–5464. doi:10.1080/01431160903369642

973 Hughes, M.J., Hayes, D.J., 2014. Automated detection of cloud and cloud shadow in single-date
974 Landsat imagery using neural networks and spatial post-processing. *Remote Sens.* 6, 4907–
975 4926. doi:10.3390/rs6064907

976 Irish, R.R., Barker, J.L., Goward, S.N., Arvidson, T., 2006. Characterization of the Landsat-7
977 ETM+ Automated Cloud-Cover Assessment (ACCA) Algorithm. *Photogramm. Eng. Remote*
978 *Sens.* 72, 1179–1188. doi:10.14358/PERS.72.10.1179

979 Jin, S., Homer, C., Yang, L., Xian, G., Fry, J., Danielson, P., Townsend, P.A., 2013. Automated
980 cloud and shadow detection and filling using two-date Landsat imagery in the USA. *Int. J.*
981 *Remote Sens.* 34, 1540–1560. doi:10.1080/01431161.2012.720045

982 Ju, J., Roy, D.P., 2008. The availability of cloud-free Landsat ETM+ data over the conterminous
983 United States and globally. *Remote Sens. Environ.* 112, 1196–1211.
984 doi:10.1016/j.rse.2007.08.011

985 Li, P., Dong, L., Xiao, H., Xu, M., 2015. A cloud image detection method based on SVM vector
986 machine. *Neurocomputing* 169, 34–42. doi:10.1016/j.neucom.2014.09.102

987 Li, Z., Shen, H., Li, H., Xia, G., Gamba, P., Zhang, L., 2017. Multi-feature combined cloud and
988 cloud shadow detection in GaoFen-1 wide field of view imagery. *Remote Sens. Environ.* 191,
989 342–358. doi:10.1016/j.rse.2017.01.026

990 Lloyd, S.P., 1982. Least Squares Quantization in PCM. *IEEE Trans. Inf. Theory* 28, 129–137.
991 doi:10.1109/TIT.1982.1056489

992 Luo, Y., Trishchenko, A.P., Khlopenkov, K. V., 2008. Developing clear-sky, cloud and cloud
993 shadow mask for producing clear-sky composites at 250-meter spatial resolution for the seven
994 MODIS land bands over Canada and North America. *Remote Sens. Environ.* 112, 4167–4185.
995 doi:10.1016/j.rse.2008.06.010

996 Lyapustin, A.I., Wang, Y., Frey, R., 2008. An automatic cloud mask algorithm based on time series
997 of MODIS measurements. *J. Geophys. Res. Atmos.* 113. doi:10.1029/2007JD009641

998 Martinuzzi, S., Gould, W., González, O., 2007. Creating cloud-free Landsat ETM+ data sets in
999 tropical landscapes: cloud and cloud-shadow removal. *Gen. Tech. Rep. IITF-GTR-32* 1–18.
1000 doi:97208-3890

1001 Platnick, S., King, M.D., Ackerman, S. a., Menzel, W.P., Baum, B. a., Riédi, J.C., Frey, R. a., 2003.
1002 The MODIS cloud products: Algorithms and examples from terra. *IEEE Trans. Geosci.*
1003 *Remote Sens.* 41, 459–472. doi:10.1109/TGRS.2002.808301

1004 Qiu, S., He, B., Zhu, Z., Liao, Z., Quan, X., 2017. Improving Fmask cloud and cloud shadow
1005 detection in mountainous area for Landsats 4–8 images. *Remote Sens. Environ.* 199, 107–
1006 119. doi:10.1016/j.rse.2017.07.002

1007 Roy, D.P., Ju, J., Kline, K., Scaramuzza, P.L., Kovalsky, V., Hansen, M., Loveland, T.R., Vermote,
1008 E., Zhang, C., 2010. Web-enabled Landsat Data (WELD): Landsat ETM+ composited
1009 mosaics of the conterminous United States. *Remote Sens. Environ.* 114, 35–49.
1010 doi:10.1016/j.rse.2009.08.011

1011 Scaramuzza, P.L., Bouchard, M.A., Dwyer, J.L., 2012. Development of the landsat data continuity
1012 mission cloud-cover assessment algorithms. *IEEE Trans. Geosci. Remote Sens.* 50, 1140–
1013 1154. doi:10.1109/TGRS.2011.2164087

1014 Wang, B., Ono, A., Muramatsu, K., Fujiwara, N., 1999. Automated Detection and Removal of
1015 Clouds and Their Shadows from Landsat TM Images. *IEICE Trans. Inf. Syst.* 82, 453–460.

1016 Wilson, M.J., Oreopoulos, L., 2013. Enhancing a simple MODIS cloud mask algorithm for the
1017 landsat data continuity mission. *IEEE Trans. Geosci. Remote Sens.* 51, 723–731.
1018 doi:10.1109/TGRS.2012.2203823

1019 Zhang, Y., Guindon, B., Cihlar, J., 2002. An image transform to characterize and compensate for
1020 spatial variations in thin cloud contamination of Landsat images. *Remote Sens. Environ.* 82,
1021 173–187. doi:10.1016/S0034-4257(02)00034-2

1022 Zhu, X., Liu, D., 2015. Improving forest aboveground biomass estimation using seasonal Landsat
1023 NDVI time-series. *ISPRS J. Photogramm. Remote Sens.* 102, 222–231.
1024 doi:10.1016/j.isprsjprs.2014.08.014

1025 Zhu, X., Liu, D., 2014. Accurate mapping of forest types using dense seasonal landsat time-series.
1026 *ISPRS J. Photogramm. Remote Sens.* 96, 1–11.

1027 Zhu, Z., Wang, S., Woodcock, C.E., 2015. Improvement and expansion of the Fmask algorithm:
1028 Cloud, cloud shadow, and snow detection for Landsats 4-7, 8, and Sentinel 2 images. *Remote*
1029 *Sens. Environ.* 159, 269–277. doi:10.1016/j.rse.2014.12.014

1030 Zhu, Z., Woodcock, C.E., 2014. Automated cloud, cloud shadow, and snow detection in
1031 multitemporal Landsat data: An algorithm designed specifically for monitoring land cover
1032 change. *Remote Sens. Environ.* 152, 217–234. doi:10.1016/j.rse.2014.06.012

1033 Zhu, Z., Woodcock, C.E., 2012. Object-based cloud and cloud shadow detection in Landsat
1034 imagery. *Remote Sens. Environ.* 118, 83–94. doi:10.1016/j.rse.2011.10.028

1035